MECHANICAL BEHAVIOR OF A CARBON NANOTUBE TURF

By

HARISH RADHAKRISHNAN

A thesis submitted in partial fulfillment of
the requirements for the degree of

MASTER OF SCIENCE IN MECHANICAL ENGINEERING

WASHINGTON STATE UNIVERSITY
School of Mechanical and Materials Engineering

December 2006

To the faculty of Washington State University:

The members of the Committee appointed to examine the thesis of HARISH RADHAKRISHNAN find it satisfactory and recommend it to be accepted.

Chair

ACKNOWLEDGEMENT

I would like to thank my committee chair and advisor, Dr. Mesarovic under whose guidance this work was conducted. His support and guidance during the past two years has been vital. I also would also like to express my gratitude to my thesis committee members, Dr. Richards C.D., Dr. William Cofer and Dr. David Bahr for their encouragement and support. The growth and the SEM images of the nanotube turf are due to Dr. Jiao and D. McClain of the Portland State University, Portland. The AFM experimental results are due to Koneswaran Sinnathamby, Haijun Ma and Christopher M. Yip of the University of Toronto. I am grateful to Professor J.A. Greenwood of the Cambridge University, United Kingdom for sending the results of his calculations for the adhesion problems thus enabling comparison with the finite element results

My sincere thanks to Coralee McCarter for the results from the mechanical testing of the turf and the many useful discussions we had regarding this research. The support from my office mates Firas Akasheh, Jagan Padbidri, Sreekanth Akarapu and Raghuraman Baskaran is greatly appreciated. I would also like to acknowledge the financial support received from the School of Mechanical and Materials Engineering for the completion of my degree. Finally a big thank you to my family back home without whose well wishes, none of this would have been possible.

MECHANICAL BEHAVIOR OF A CARBON NANOTUBE TURF

Abstract

by Harish Radhakrishnan, M.S.
Washington State University
December 2006

Chair: Sinisa Dj. Mesarovic

Carbon nanotubes grown on a substrate form a *turf* – a complex structure of intertwined, mostly nominally vertical tubes, cross-linked by adhesive contact and a few bracing tubes. The mechanical behavior of such a turf is analyzed and the physical mechanism of deformation deduced on the basis of (a) experimental results – standard and continuous stiffness nanoindentation tests and (b) micromechanical scaling analysis. The objective here is to develop a phenomenological model to simulate the behavior of the turf in nanoindentation tests, taking into account the various features observed during the experiments.

Under moderate strains and deformations, the turf is fully reversible (non-linear elastic response) with a small Kelvin-Voigt type relaxation. Also observed in the experiments is the strong adhesion between the turf and indenter tip – due to the van der Waals forces of attraction. A finite element model has been developed and is able to reproduce the results from the indentation tests with reasonable accuracy.

While the adhesive contact in the indentation of linear elastic solids is thought to be well understood through analytical models, a finite element model for the problem is yet to be developed. To benchmark the developed contact algorithm, runs were done to compare the results with existing theories of adhesion. The comparison revealed an unanticipated deviation from the existing models and is thought to be due to the finite deformation in the elastic material, not considered by the existing theories.

TABLE OF CONTENTS

LIST OF FIGURES

LIST OF TABLES

CHAPTER 1

INTRODUCTION

Since their discovery in the early nineties, carbon nanotubes have been the focus of several studies. Carbon nanotubes are purported to have excellent mechanical, electrical and thermal properties [3] making them suitable for nanoscale sensors and devices. While there is a substantial amount of work done on analyzing the properties of nanotubes, [3, 4, 20, 21, 24, 25 and 26] challenges still need to be overcome for successfully exploiting their superior properties in *working* devices. To date, the collective mechanical properties of carbon nanotubes have been analyzed only for short, widely spaced tubes [21, 22 and 25]. The objective of the current work is to study the collective mechanical behavior of carbon nanotubes interacting with each other through

1) Nanoindentation experiments
    a. Standard indentation experiments – to study the load-depth response of the turf
    b. Dynamic stiffness measurements – to measure the tangent modulus of the turf as a function of indentation depth
2) A micromechanical model which serves to explain the mechanism of deformation in the structure.
3) Development of a phenomenological model based on experimental observations.

An effort is also made to benchmark the developed finite element model with the established theories of adhesion.

Carbon nanotubes grown on a substrate form a *turf* [1], a complex structure of intertwined, mostly nominally vertical tubes, cross-linked by adhesive contact and a few bracing tubes (fig 1.1). The turf grown by chemical vapor deposition (CVD) with a sol-gel catalyst is compliant and expected to act as good thermal conductor – thus a promising contact switch material for a MEMS device [14, 17].

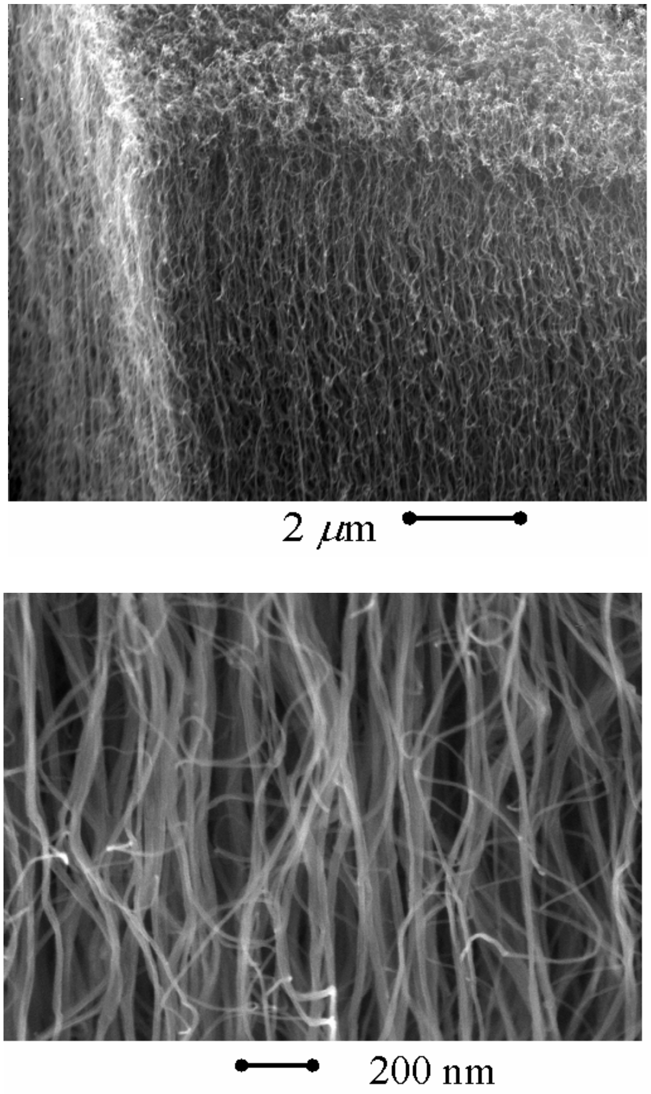

Fig 1.1: Carbon nanotube turf (top) a corner view (bottom) detail [17]

---

[1] There is no consistent term for the collective form of nanotubes grown on a substrate. In certain cases, they are referred to as 'Vertically aligned carbon nanotube forest' (VACNT) [20]. Here the name is based on its resemblance to a 'grass-turf'.

As evident from the fig 1.1, most nanotubes in the turf are nominally vertical and slightly curved, while some segments are inclined or even horizontal. The contacts are likely van der Waals bonded. Nanotubes have a high surface energy in air and low interface energy, so that the system lowers its energy by contact. If nanotubes are prevented from moving during growth, the contact requires bending of the tubes which increases the strain energy, *U*, of the assembly. The total energy in the assembly, *E*, can be written as the sum of elastic energy and contact energy, Γ.

$$E = U - \Gamma \qquad \ldots (1.1)$$

where the Γ is taken as the difference between total interface energy of the assembly and an imaginary contact-free assembly. The configurational space is large, so that many local energy minima are expected. However, experimentally observed mechanical reversibility indicates that the energy functional has broad convex regions around the energy minima, so that the structure is expected to return to its initial state after deformation. The absolute energy minimum for the configuration is when all the tubes collapse laterally so that the entire length of the nanotube is in contact with adjacent tubes. The assumed existence of the energy function serves as the basis for the development of the micro-mechanical model. While the final goal would be to determine a relationship between the parameters in the micro-mechanical model and an equivalent continuum model, the current analysis is simplified based on two assumptions a) material isotropy and b) high compressibility.

The thesis is organized as follows: In the second chapter, the experimental results and the development of a rudimentary micro-mechanical model are discussed. The development of the micro-mechanical model is based on the observed mechanical reversibility in the experiments and serves to explain the basic mechanism of deformation in the turf. The third chapter deals with the established theories of adhesion. They serve to benchmark the developed finite element model and also aid in the interpretation of the results from the nanoindentation experiments. The fourth chapter is concerned with the development of a phenomenological model for the nanotube turf. The turf is treated as isotropic nonlinear elastic material with time dependent relaxation and an appropriate contact law to simulate the strong adhesion. In the final chapter the results from finite element analysis are broadly discussed in two categories. The discussion on the results regarding adhesion in linear elastic solids is followed by results from the analysis of spherical indentation on the carbon nanotube turf.

CHAPTER 2

OVERVIEW OF THE MECHANICAL BEHAVIOR OF THE CARBON NANOTUBE TURF

(This chapter is taken from [17] with minor changes)

The deformation of both single and multi-walled carbon nanotubes have been studied for some time using molecular dynamics [3] and an equivalent continuum model using shell theory [20]. In contrast, the analysis of deformation in a nanotube turf has only been studied recently and has been restricted to short, widely spaced tubes [21, 25]. The objective here is to gain a better understanding of the deformation in a complex nanotube turf using experimental results and a micro-mechanical model.

2.1 Nanoindentation experiments on vertically aligned carbon nanotubes – A review

Nanoindentation experiments are often used to assay the mechanical properties of materials in small volumes. Existing nanoindentation experiments on short widely spaced nanotubes focus on determining the mechanical properties of individual nanotubes. Qi et al [21] used a conical diamond indenter to obtain a statistical measure of the effective bending stiffness and elastic modulus of multi-walled carbon nanotubes. Similarly Waters et al [25] studied the buckling of short multi-walled carbon nanotubes (50-100nm) through indentation with a circular flat punch. These experiments served to examine the applicability of continuum theories (beam theory and linear elastic thin shell model) in studying the deformation of multi-walled carbon nanotubes.

Recently there has been an interest in studying the mechanical properties of interacting tubes as a 'Super-compressible' ultralight foam structure [4]. The structure is reported to retain its original configuration even after the removal of the bottom substrate. Under compression the nanotubes buckle but are completely reversible up to large strains (15% of the original height). The recovery of the total height of the structure is reported to last hundreds of cycles of compression and the load – depth response under compression was identical to that of elastomeric foams. The above mentioned mechanical properties and the large thermal conductivity of carbon nanotubes [3] make such a structure a suitable candidate as a contact material for a MEMS device [14, 17].

2.2 Experimental Observations – standard nanoindentation experiments

In the current analysis, indentation tests were performed using a Hysitron triboscope with a mechanism as seen in fig 2.1a. The indentation is a force-controlled type of experiment where P is the controlled force applied and due to the compliance of the indentation mechanism, the actual force Q on the turf is slightly different. The results from standard nanoindentation experiments are shown in fig 2.2. A blunt Berkovich indenter with a tip radius of about 1.8 μm is used. The indenter is spherical up to a depth of 100 nm after which the cross-sectional area is triangular.

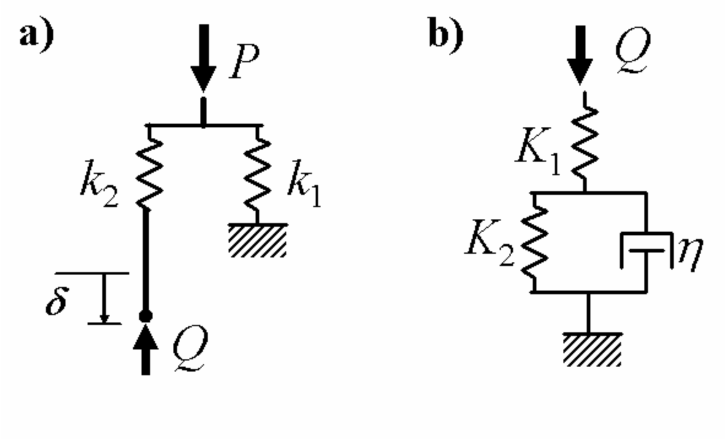

Fig 2.1: a) Symbolic representation of the nanoindentation mechanism b) Quasi-rheological model of the indentation experiment [17].

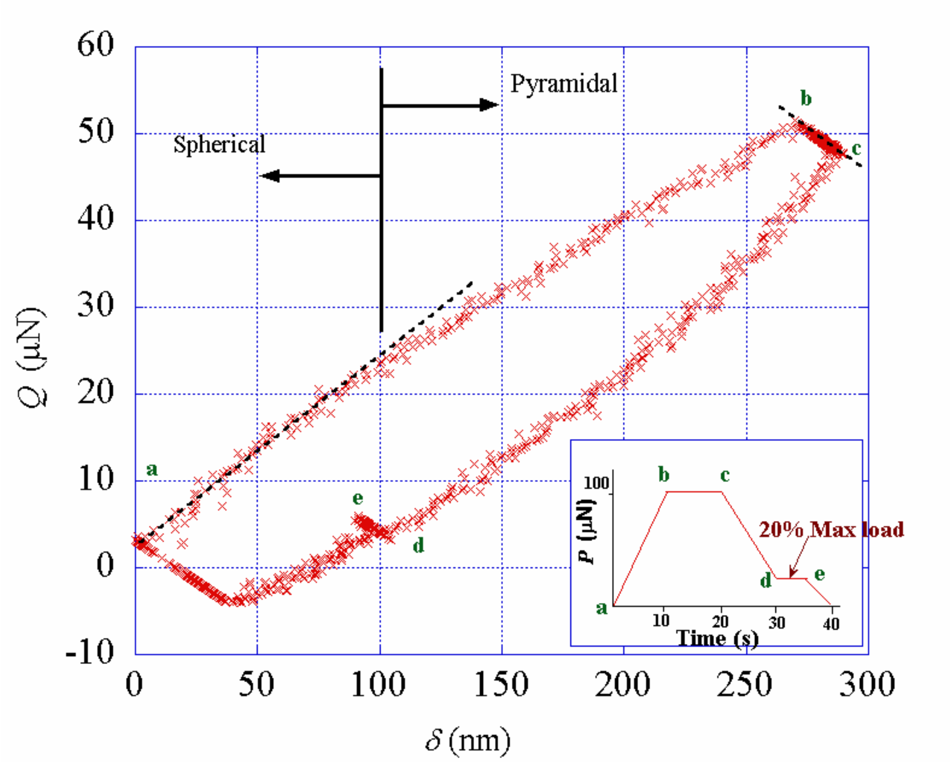

Fig 2.2: True force, Q–displacement, δ curve for the given loading schedule, P-inset [17].

From the results from the standard nanoindentation experiment, the following can be summarized

a) The deformation is completely reversible indicating that the turf exhibits elastic behavior (or more specifically non-linear elastic behavior).

b) The force-depth relation during the indentation with the spherical portion (<100 nm) is linear. Thus the appropriate quasi-rheological model[2] (force-displacement relation) is linear viscoelastic, where the top spring with stiffness K_1 ensures an instantaneous response to a step load (fig 2.1b).

c) During the constant load segment (segment b-c), the turf exhibits time-dependent relaxation. The total relaxation of the material is small, hence the spring $K_2 >> K_1$.

d) Finally, while retracting the indenter from the turf, the tip experiences strong adhesion (seen as the tensile load – a portion of segment e-a) owing to the compliant nature of the turf.

The time dependent relaxation of the turf is surprising as the deformation of carbon nanotubes are not history dependent. Further, the separation of contact in two adjacent tubes is analogous to crack propagation, once again a time independent phenomenon. Perhaps the only mechanism to explain this feature is the thermally activated sliding of contacts between the tubes.

A well known contact mechanics result is that a linear force-displacement relation in the loading part of the cycle is expected for spherical indentations of elastic-ideally plastic material. This response of the turf is puzzling, in that the nanotubes are expected to be elastic. The strong adhesion between the turf and the indenter surface is due to the high surface energy of the nanotubes in air, the compliant nature of the turf and the near

---

[2] This model is not a constitutive law for the material.

perfect geometry of each nanotube[3] allowing intimate contact between the contacting surfaces.

2.3 Indentation law

To obtain the quasi-rheological constants K_1, K_2 and η (fig 2.1), it is necessary to solve the combined machine and indentation models. The interest lies in obtaining the expressions for $dQ/d\delta$, for the various segments of the experiment. The experiment involves constant force and constant force rate segments. For the loading of the type

$$P(t) = P_0 + \dot{P}t \qquad \dots\ 2.1$$

and with an initial indentation depth h_0, the general solution can be written as

$$\omega\eta \cdot d\delta/dt = \left(P_0\psi - \dot{P}\tau\zeta - \delta_0\omega\eta/\tau\right)e^{-t/\tau} + \dot{P}\tau\psi \qquad \dots\ 2.2$$

$$\omega\eta \cdot dQ/dt = \chi\left(P_0\psi - \dot{P}\tau\zeta - \delta_0\omega\xi/\tau\right)e^{-t/\tau} + \dot{P}\tau K_2 \qquad \dots\ 2.3$$

where

$$\begin{aligned} 1/\chi &= 1/k_1 + 1/k_2 \\ \omega &= k_1\left(1/\chi + 1/K_1\right) \\ 1/\zeta &= 1 + \chi/K_1 \\ \psi &= 1 + K_2/K_1 \end{aligned} \qquad \dots\ 2.4$$

The characteristic relaxation time can be determined by

$$\tau = \eta/\left(k_1/\alpha + K_2\right) \qquad \dots\ 2.5$$

For the relaxation during constant load segments, $dP/dt\ = 0$

---

[3] Nanotubes can be considered as seamless cylinders formed by the rolling of planar graphite sheets [3].

$$dQ/d\delta = \chi \qquad \ldots\ 2.6$$

Therefore the relaxation slope is a machine property. During the initial loading P_0, δ_0 are zero and assuming $K_2 >> K_1$

$$dQ/d\delta \approx K_1 \qquad \ldots\ 2.7$$

2.4 A micro-mechanical model

The structure of the nanotube turf is very complex and the current goal is to determine the dominant mechanisms. The model developed serves a limited purpose for identifying the mechanism and establishing the basic scaling laws. During the indentation of the turf, much of it is loaded in compression along the axes of the nanotubes and hence the focus is on the compression of the tubes. In this case, load is carried by the nominally vertical tubes while the inclined and horizontal tubes brace the structure (fig 1.1).

As evident from the figure and equation 1.1, the carbon nanotube turf has a certain amount of strain energy locked in. This is balanced by lowering the total energy in the turf through contacts. Let the total length of the nominally vertical tubes per unit mass be L. The length can be divided into n typical contact patches and n typical free segments.

$$L = nl + na$$

The length of the contact patch 'a' is assumed to be straight, constant and does not contribute to the deformation. This argument is based on the reversibility of the deformation which allows the consideration of the deformation under constant structure (constant contact). The strain energy in the turf can then be expressed in terms of average (absolute) curvature of the free segments, κ:

$$U = \frac{1}{2} nlK\kappa^2 \qquad \ldots 2.8$$

Here K is the bending stiffness of the nanotubes. Strictly speaking, the strain energy is dependent on the mean square of the curvature of the free segments. In the current case, this is ignored. The contact energy γ is the work required to separate a contact between two nanotubes, given per unit length of the contact, or the difference between the surface energy of a nanotube in air and interface energy between two nanotubes. The total energy density per unit mass of the of the system is then

$$E = \frac{1}{2} n\ell K\kappa^2 - \frac{1}{2} na\gamma \qquad \ldots 2.9$$

For scaling purposes, a geometrical analysis of segment with constant curvature (fig 2.3) is considered.

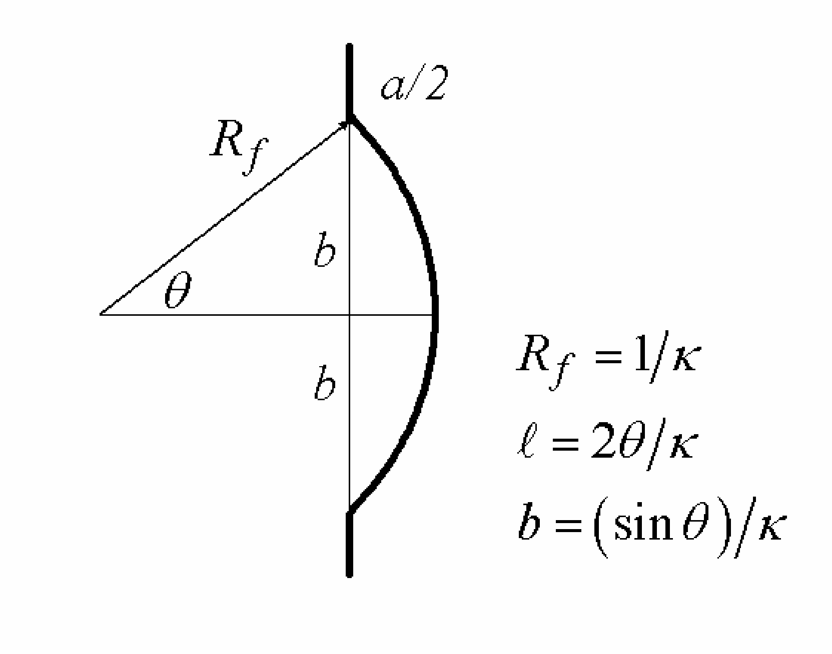

Fig 2.3: A typical free segment with an initial curvature [17]

Considering a small strain increment, $\delta\varepsilon$, positive in compression

$$\delta\varepsilon = \frac{-\delta b}{b + a/2} \qquad \ldots\ 2.10$$

The deformation is taking place under constant structure, i.e., constant ℓ. The strain and the curvature are then related as

$$\kappa f(\theta)\delta\varepsilon = \delta\kappa \qquad \ldots\ 2.11$$

where

$$f(\theta) = \frac{\phi\theta + \sin\theta}{\phi\cos\theta - \sin\theta} \qquad \ldots\ 2.12$$

with $\phi = a/l$.

The stress, positive in compression is:

$$\sigma = \frac{\partial E}{\partial \varepsilon} = \frac{\partial E}{\partial \kappa}\frac{\partial \kappa}{\partial \varepsilon} = n\ell K\kappa^2 f(\theta) \qquad \ldots\ 2.13$$

The existence of the threshold stress is evident:

$$\sigma_0 = N\ell K{\kappa_0}^2 f(\theta) \qquad \ldots\ 2.14$$

As soon as a small strain $\varepsilon \sim 0$ is applied, the stress jumps to the value σ_0. In other words, no compressive strain occurs below this value of stress. In the real material, the transition is gradual since there is a distribution of segment lengths and initial curvatures present.

As an aid to intuition, consider the analogy with a tautly strung bow – little deformation is accomplished by a force too weak to slacken the string. In the present case, the contact energy plays the role analogous to the string strain energy. Further insight can be gained from observation that the free segment in fig 2.3 behaves as a prebuckled elastica[4] with a relatively small tangent stiffness. Therefore, for small compressive axial strains and monotonic loading, the behavior is expected to be similar to elastic – ideally plastic or mildly strain-hardening material i.e. a high initial tangent modulus followed by a significantly lower tangent modulus beyond the threshold stress. The depth sensing experiments (continuous-nanoindentation experiments) confirm the expectations. The experiments indicate that the tangent modulus decreases with indentation depth by an order of magnitude.

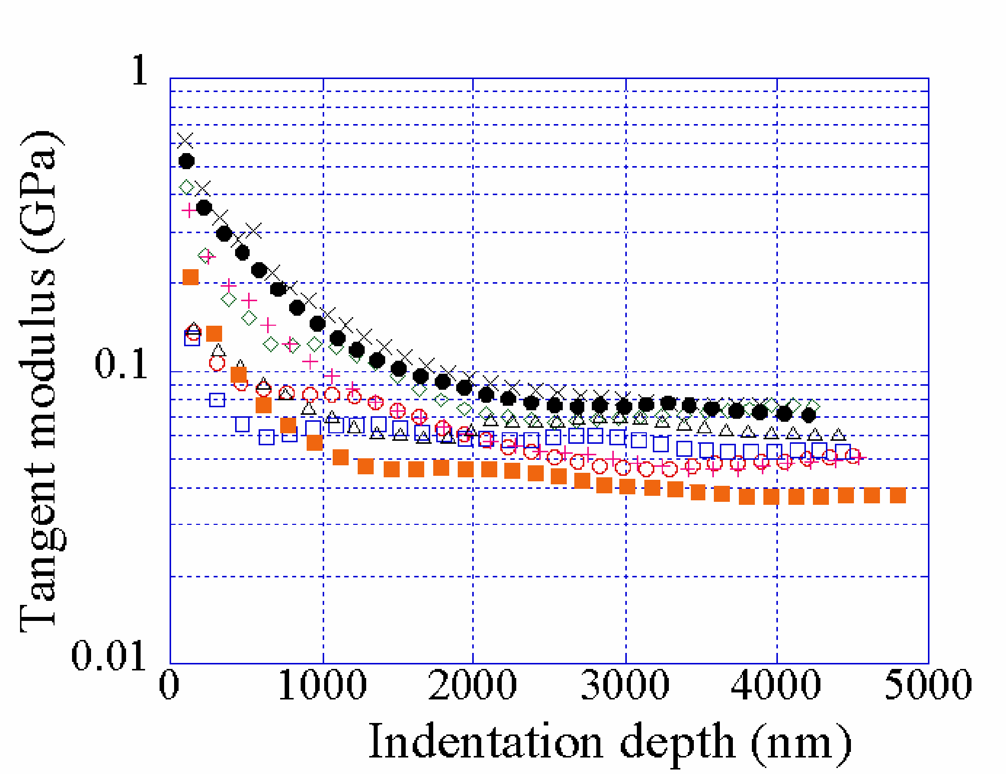

Fig 2.4: Depth sensing indentation experiments on a CNT turf. Indentations are taken at different distances from the edge of the turf. The more compliant cases correspond to the indentations close to the edge. [17]

---

[4] The spatial elastica can be defined as a model of an elastic rod, used in the analysis of geometrically non-linear deformations in three dimensions [18]

CHAPTER 3

CONTACT MECHANICS AND ADHESION IN SOFT ELASTIC SOLIDS

Any analysis of the indentation experiments on the carbon nanotube turf should take into account the strong adhesion between the turf and the indenter tip. These strong interactions are due to the van der Waals forces acting between the two surfaces. While the problem at hand has material, geometric, and contact nonlinearities, a simplified problem involving adhesive contact in linear-elastic solids is studied first. The adhesive contact between two elastic spheres has been the subject of several studies with notable contributions made by Johnson [7, 10, 11 and 12], Derjaguin [5], Greenwood [6, 7, and 12] and Maugis [13]. While analytical solutions [5, 7, 10 and 13] and numerical (finite-difference) results [2, 6] exist, a finite element model is still lacking and the development of such a model forms the initial part of the investigation.

3.1 JKR theory of adhesion

An analysis on the adhesion in elastic spheres by Johnson, Kendall and Roberts (JKR) [10] sought to explain the discrepancies between experiments and the classical Hertz theory. Experiments showed that, at low loads, the contact radius is greater than that predicted by the Hertz theory and this anomaly was attributed to the adhesive forces acting between the contacting surfaces (they are neglected in the Hertz theory of contact). The JKR theory is based on this experimental evidence and modifies the existing Hertz results to account for these adhesive forces.

The classical Hertz theory of contact [11] shows that when two elastic spheres of radii R_1 and R_2 are pressed together with a load *P*, the radius of contact a_0 can be expressed by

$$a_0{}^3 = \frac{3\pi RP}{4E^*} \qquad \text{… (3.1)}$$

The effective plane strain modulus, *E** is given by

$$\frac{1}{E^*} = \frac{1}{E_1{}^*} + \frac{1}{E_2{}^*} = \frac{1-\nu_1{}^2}{E_1} + \frac{1-\nu_2{}^2}{E_2} \qquad \text{... (3.2)}$$

where v_i is the Poisson's ratio, E_i the Young's modulus of the materials and $R = R_1 R_2 / (R_1 + R_2)$ is the effective radius of the spheres[5]. As the contact radius is much smaller than the radius of the spheres (Hertz theory is valid for small strains, i.e. $a_0/R < 0.15$ [16]), the profile can be approximated as a paraboloid and distant points in the two spheres can be shown to approach each other by a distance δ, where

$$\delta = a_0{}^2 / R \qquad \text{... (3.3)}$$

The JKR theory is based on the balance between the strain energy (calculated using Hertz's results), mechanical energy, and surface energy (energy required to create new surfaces) – similar to that of the Griffith model of brittle cracks. Considering adhesion, the modified contact radius *a* is then given by

$$a^3 = \frac{3\pi R}{4E^*}\left(P + 3\gamma\pi R + \sqrt{6\gamma\pi RP + \{3\gamma\pi R\}^2}\right) \qquad \text{… (3.4)}$$

where γ is the energy of adhesion between the surfaces (units J/m^2). Evidently, even at zero applied load, the contact radius is finite.

---

[5] A situation one most likely would encounter involves a rigid sphere ($R_1 = R$; $E_1{}^* = \infty$) and a deformable half space ($R_2 = \infty$; $E_2{}^* = E^*$) so that the effective radius of the spheres is *R* and effective plane strain modulus is *E** - Spherical indentation problem

$$a^3 = \frac{9\pi^2\gamma R^2}{2E^*} \quad \text{at} \quad P = 0 \qquad \ldots (3.5)$$

The complete separation of contact occurs when a pull-off-load[6] of magnitude

$$P_{pull-off} = -\frac{3}{2}\pi R\gamma \qquad \ldots (3.6)$$

is applied. An interesting aspect is that the pull-off load is independent of the elastic modulus and thus implies that the model is valid for both rigid as well deformable spheres. While the JKR theory predicts an infinite tensile traction at the contact edge (fig 3.1), Johnson et al speculate that the edges should separate slightly so that the deformed surface profile is smooth and the stresses fall to a finite value.

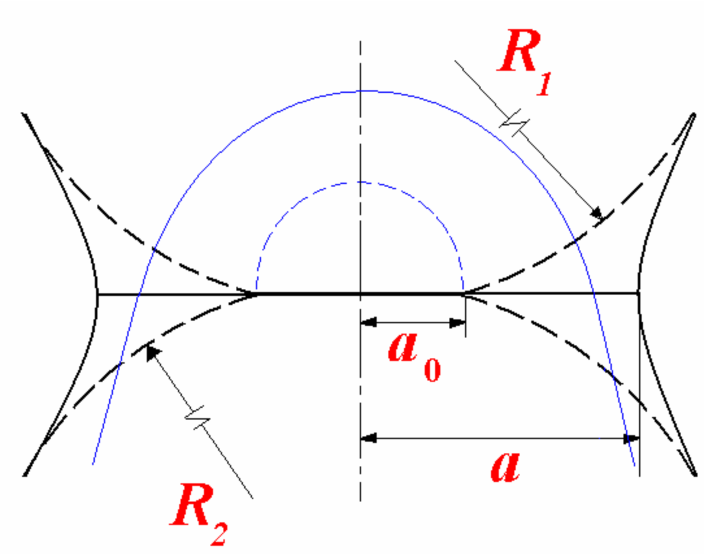

Fig 3.1: Contact between elastic spheres, *black* lines – profile of the deformed spheres, *blue* lines – traction distribution across the contact surface [10]. **Note** (i) The deformed profile changes from one that meets the interface tangentially (broken line – Hertz theory) to one that meets perpendicularly (solid line – JKR theory) (ii) The infinite tensile traction and sharp discontinuity at the contact edge predicted by JKR theory.

---

[6] The pull-off load is the magnitude of tensile load needed to completely separate two contacting spheres which are under the influence of adhesive forces.

3.2 DMT Theory

Shortly after JKR theory was proposed, an alternate theory by Derjaguin, Muller and Toporov (DMT) [5] seeking to explain the same phenomenon but with a different set of assumptions was put forward. Here the attractive forces outside the contact radius are considered (not so in the JKR theory, which is a surface analysis approach) but the deformed profile is still assumed to be Hertzian as if the material were stiff enough to prevent deformation. The DMT model predicts a pull-off force of magnitude

$$P_{pull-off} = -2\pi R\gamma \qquad \ldots (3.7)$$

Strangely, the pull-off force, similar to the JKR theory, is independent of the elastic modulus although the constant changes. This discrepancy between the two theories was settled by Tabor [23] when he showed that the assumptions made by the two theories restrict their validity and the appropriate regimes of each model could be best mapped by an elastic parameter 'μ' commonly referred to as the Tabor's non-dimensional parameter. Tabor noted that at zero load, the height *h*, of the neck around the contact edge can be shown as

$$h \propto \left(\frac{R\gamma^2}{E*^2} \right)^{1/3} \qquad \ldots (3.8)$$

If this height is of the order of the inter-atomic spacing (α_0), then the adhesive forces outside the contact perimeter must be accounted for (DMT theory) and on the other hand when the height is greater than α_0, they could be neglected (JKR model). An obvious dimensionless parameter is obtained by normalization of this height with α_0.

$$\mu = \left(\frac{R\gamma^2}{E^{*2}\, \alpha_0{}^3} \right)^{1/3} \qquad \ldots (3.9)$$

The resulting non-dimensional parameter μ can be thought of as the elastic displacements in the deformable half-space due to the adhesive tractions, normalized by the range of these forces. Clearly, the DMT theory is valid for low μ (<0.1), while the JKR theory is valid for large μ (>5) [12].

3.3 Maugis–Dugdale model

While Tabor was able to show that the existing theories occupied the ends of the spectrum represented by the parameter μ, analysis demonstrating the transition still remained. Adhesion in elastic solids is a special problem where surface physics, contact mechanics, and fracture mechanics are mixed in an intricate manner. This feature was exploited by Maugis [13], where he effectively combined (superimposed) the stresses due to indentation of an axis-symmetric punch in an elastic half-space with the stresses in a external, axis-symmetric Dugdale crack. While the individual solutions have singularities at the contact/crack edge, these cancel out, resulting in the continuity of the stress (the earlier JKR model showed a stress-discontinuity at the contact edge). In the Maugis model, the material at the periphery of the contact is assumed to have failed at the theoretical strength (σ_0). Introducing the non-dimensional parameters[7] by Maugis [7],

---

[7] While the Tabor parameter μ implies the use of an idealized Lennard-Jones force-separation law, in the Maugis model, the compressive forces are merged with bulk elasticity while the tensile tractions are specified separately. Hence, the elastic non-dimensional parameter, λ introduced by Maugis is different and it reflects the above change. For a 9-3 Lennard-Jones potential, $\lambda = 1.16\mu$.

$$\bar{a} = a\beta \; ; \; \bar{c} = c\beta \; ; \; \beta = \left(\frac{4E^*}{3\pi\gamma R^2}\right)^{1/3}$$

$$\bar{P} = P/\pi\gamma R \; ; \; \lambda = \sigma_0 \left(\frac{9R}{2\pi\gamma E^{*2}}\right)^{1/3} \qquad \ldots (3.10)$$

For a given load P and elastic parameter λ, the other unknown variables can then be computed by solving the two simultaneous equations below.

$$\frac{\lambda \bar{a}^2}{2}\left\{(m^2-2)\sec^{-1}(m)+\sqrt{m^2-1}\right\}+\frac{4\lambda \bar{a}^2}{3}\left\{\sqrt{m^2-1}\sec^{-1}(m)-m+1\right\}=1$$

$$\bar{P} = \bar{a}^3 - \lambda \bar{a}^2\left\{\sqrt{m^2-1}+m^2\sec^{-1}(m)\right\} \qquad \ldots (3.11)$$

where $m = c/a$, $(c-a)$ is the annulus over which the tensile stress σ_0, is constant. Expectedly as $\lambda \to \infty$; $c \to 0$, implying the progressive reduction in the annulus width. The advantage of the Maugis model is that the solution is portable i.e. valid for all values of μ.

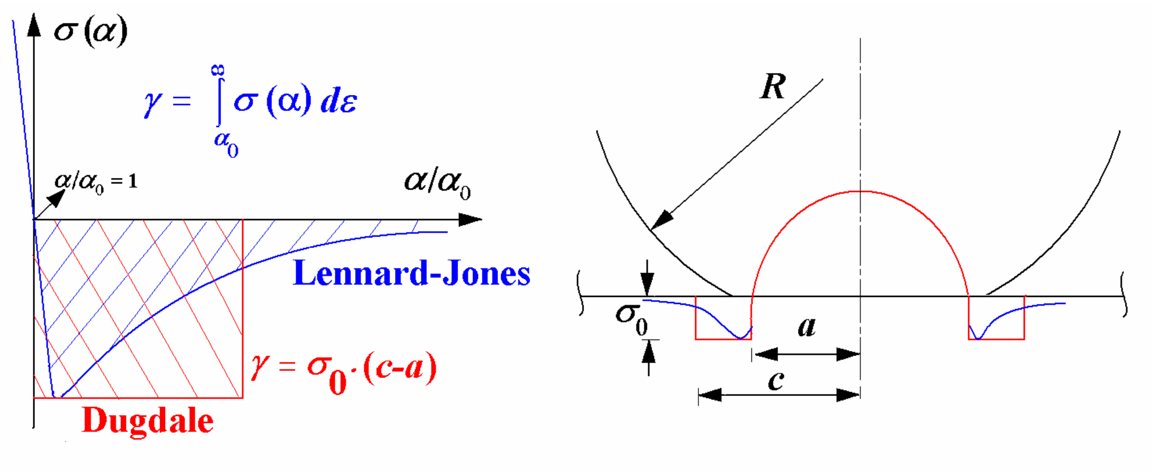

Fig 3.2: a) Force separation laws b) Traction distribution [12]

Other models demonstrating a similar transition include numerical (finite difference) solutions by Greenwood [6] and a double Hertz model by Greenwood & Johnson [7]. In Greenwood's numerical results, an idealistic Lennard-Jones type force separation law was used. A feature common to all existing models is the assumption that the deformation gradients are small (linear geometry).

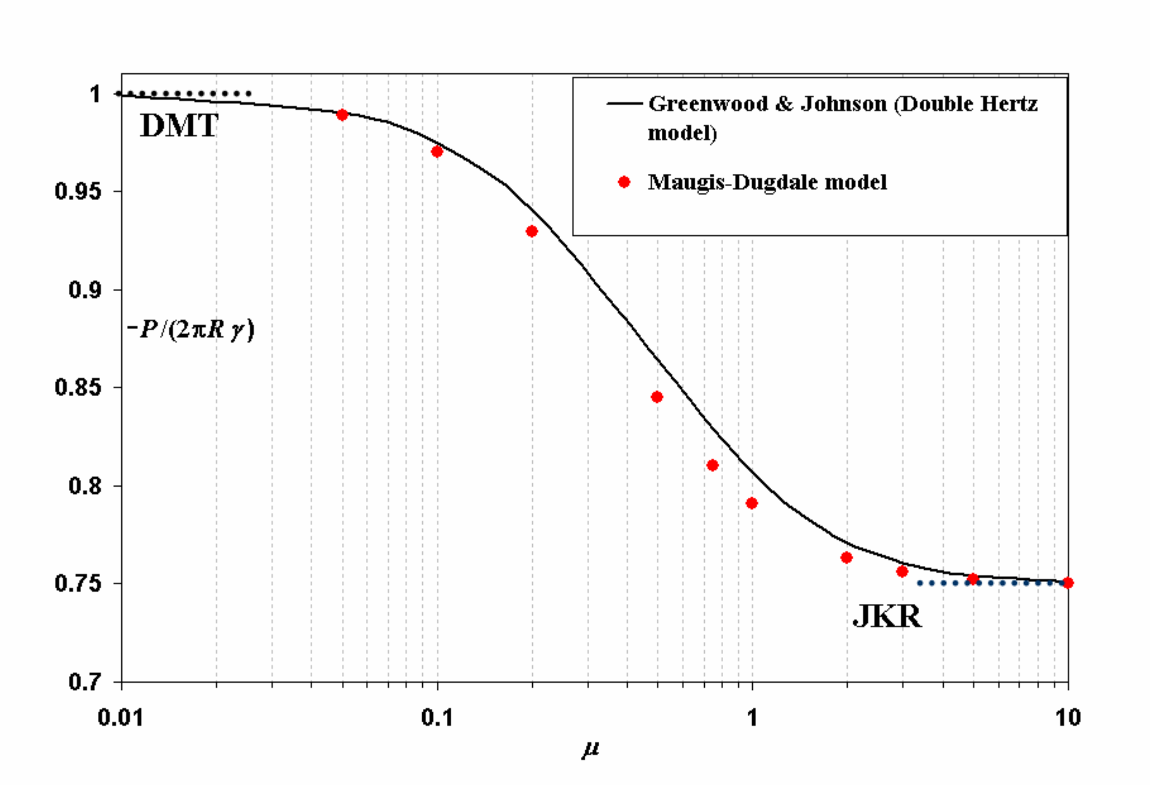

Fig 3.3: The transition from DMT model to JKR model – Pull-off load values

CHAPTER 4

FINITE ELEMENT ANALYSIS OF CONTACT PROBLEMS

When contact problems are analyzed through the finite element technique, there are errors specific to the problem. These errors are mesh-dependent and the nature/source was analyzed earlier by Mesarovic and Fleck [15]. In general, these are errors in the estimation of the contact radius (due to the discretisation of the domain) and in the measurement of indenter load (due to additional inherent errors in the FE technique, e.g. element interpolation functions). The magnitude of these errors is thus dependent on the size of the mesh.

4.1 Mesh details

In the current analysis, the elastic half-space is discretised using 3-noded axis-symmetric triangular elements (CST –constant strain triangle element). While higher order elements are usually preferred in finite element analysis, the mesh in the current analysis is very dense close to the contact area. Higher order elements (6-noded triangular) proved to be computationally expensive and provided no noticeable difference in the results when compared with the CST element. The element size close to the contact surface is of the order of inter-atomic spacing while elements distant from the surface are significantly larger (fig 4.1, 4.2). The total width of the elastic half space is taken to be ten times the size of the contact radius. This is a common practice for contact problems and is done to ensure that the boundary conditions do not influence the stresses due to contact [15].

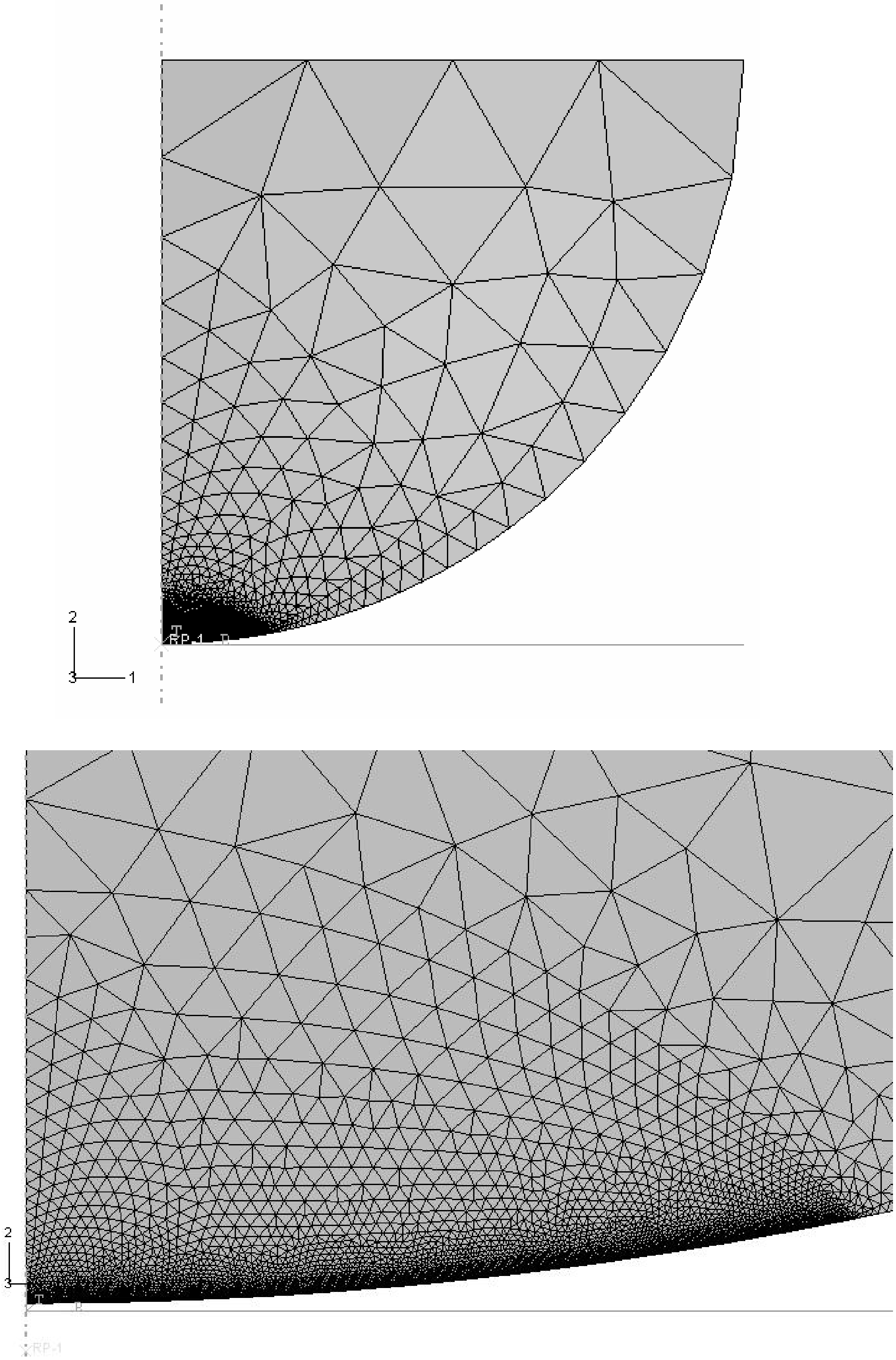

Fig 4.1: Mesh details – deformable linear elastic sphere (10,305 CST elements, 16,461 dof's). Area of smallest element: 0.05 nm^2, largest element: 27.5x10^3 nm^2

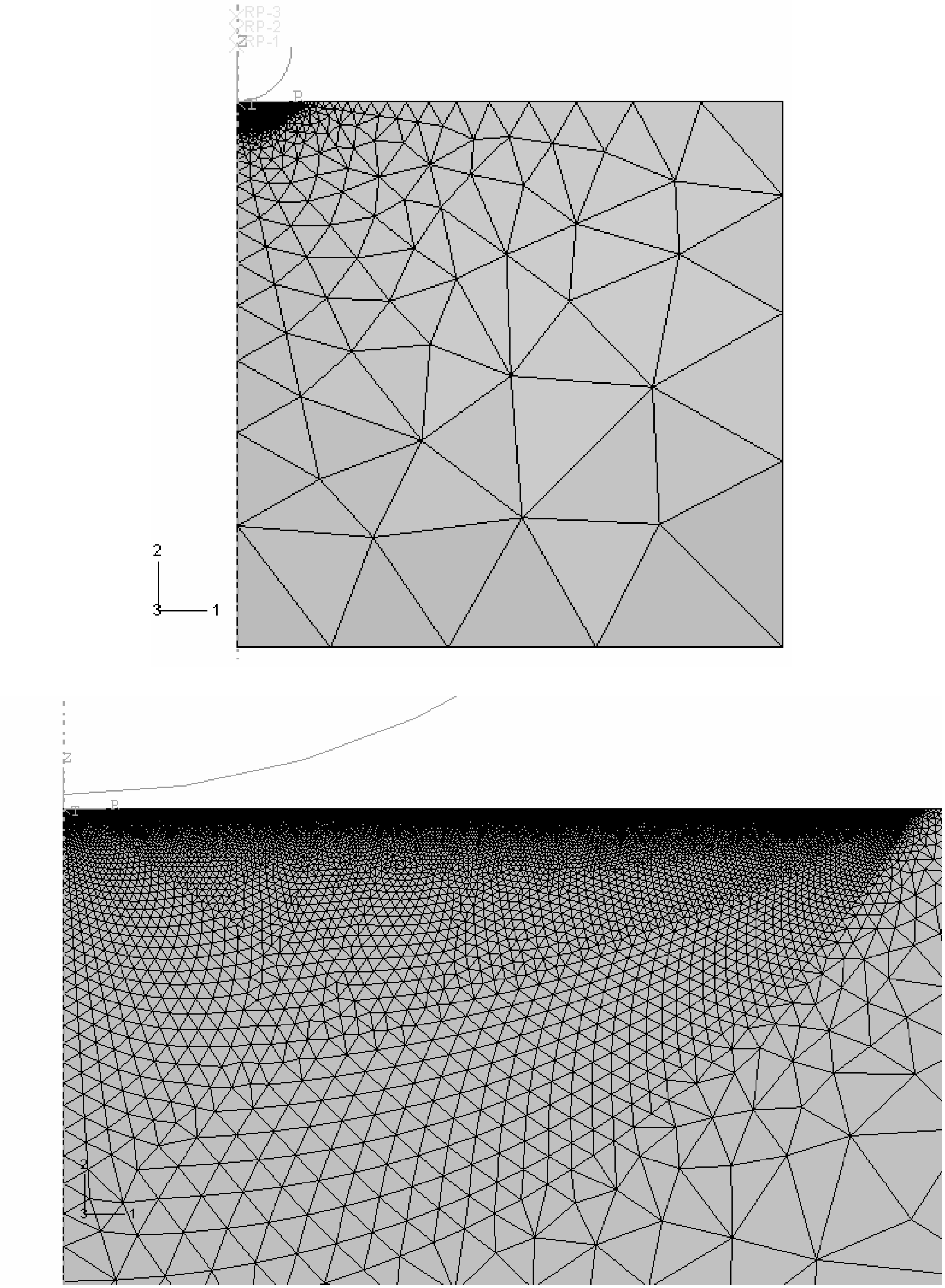

Fig 4.2: Mesh details – Nanotube turf (28,397 elements, 44,118 dof’s). Area of smallest element: 1.851 nm^2, largest element: 14.96x10^6 nm^2

4.2 Contact algorithm

The contact between the elastic half-space and the rigid indenter is specified by the tractions, ***t*** – calculated using the Lennard Jones (LJ) potential, acting across the surface and are a function of the shortest distance (α) between the slave node (half-space) and master surface (indenter). The LJ potential is originally intended for simulating the van der Waals interaction between atoms where the traction ***t***, is directed along an imaginary line joining the interacting atoms.

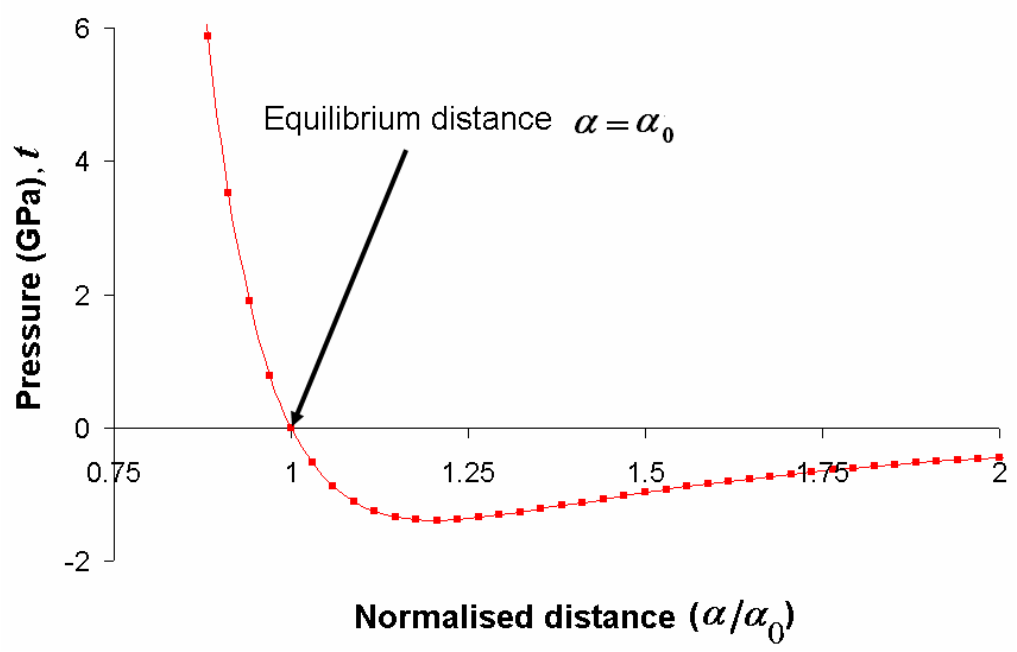

Fig 4.3: Force-separation law (LJP 9,3)

$$t(\alpha) = \left(\frac{8\gamma}{3\alpha_0}\right)\left(\left(\frac{\alpha_0}{\alpha}\right)^3 - \left(\frac{\alpha_0}{\alpha}\right)^9\right) \qquad \ldots (4.1)$$

The force-separation law (equation 4.1) used is identical to Greenwood's earlier analysis [6] (Lennard Jones potential - LJP, with power 9,3). The use of a non-default contact law in ABAQUS required the development of a separate user defined subroutine, UINTER

[1]. Typical inputs to the subroutine are the current interfacial distance $\left(\alpha_j\right)$ between the slave node and master surface and its increment $\left(\Delta\alpha_j\right)$. The outputs are the tractions $\left(t_i\right)$ and the appropriate Jacobian terms $\left(\partial t_i/\partial\alpha_j\right)$.

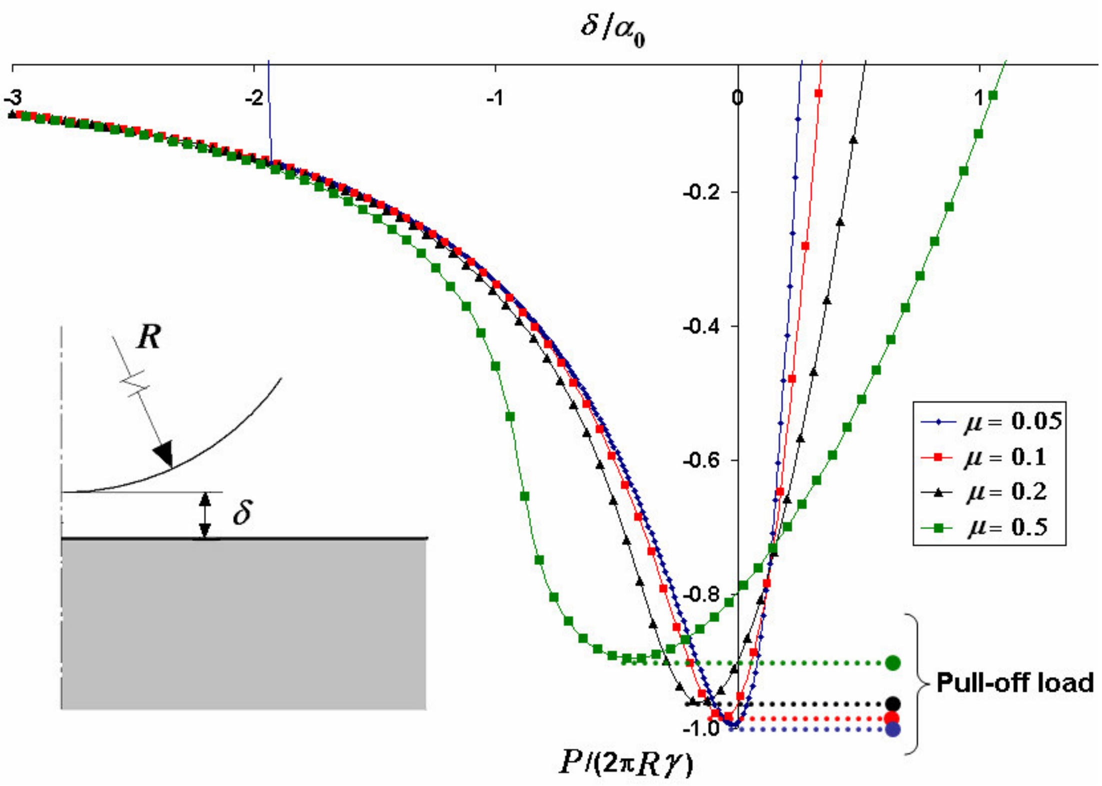

Fig 4.4: Finite element analysis results: Load-depth curves[8] for low values of μ.

As expected, the results from finite element analysis (fig 4.4) show that the magnitude of the non-dimensional pull-off load, initially close to that predicted by the DMT theory, decreases with increasing μ. Another key feature is the increasingly steeper slopes of the load-displacement curve when approached from afar. Physically, this refers to a rapid

---

[8] The sign convention for load and displacement are made consistent with existing literature. Positive loads (P) indicate compression while negative loads tension. Positive distances (δ) indicate penetration and negative distances, clearance between the surfaces – approach of the sphere from far to zero force position

transition from a state without contact to contact[9] and such transitions are difficult to handle numerically.

While the Newton-Raphson method is robust and commonly used to solve non-linear problems, it requires the global stiffness matrix to be positive definite. During the transition, this requirement is not met and the solution can either be obtained by using a Riks method or modifying the Newton-Raphson method to include external damping (force convergence). The latter method was preferred as the size of the time increment required to solve by the Riks method progressively reduces with larger μ and thus becomes computationally expensive. Nevertheless, a few additional runs were done by Riks method to ensure the validity of the solution obtained by damping (fig. 4.6).

4.3 Viscous damping

During the jump-to-contact portion, the unstable nodes tend to attain a high velocity and a viscous force applied in the opposite direction dampens their motion. There are two ways to apply viscous damping a) part of the global equilibrium equations b) part of the contact pressure definition. In the former case the global equilibrium equations are

$$F_e - F_i - F_v = 0 \qquad \ldots (4.2)$$

where F_e are the external forces, F_i are the internal forces and F_v are the viscous forces calculated at each node.

$$F_v = c \cdot M^* \cdot v \qquad \ldots (4.3)$$

---

[9] During the transition the contact radius jumps from zero to a finite value for a small perturbation in the indenter load (load jumps – fig 4.6). This condition is referred to as jump-to-contact. The feature first appears for a value $\mu = 0.75$ (contact law using LJP 10,4).

c is the viscous damping co-efficient (units s^{-1}), M^* is the mass of each element associated with the node (calculated by assuming the elements to be of unit density) and v is the velocity of the node. This method produced erroneous solutions as the damping was never enforced properly – the unstable nodes are at the surface of the material but the damping is applied throughout the elastic half-space resulting in a large ratio of the damped energy to the strain energy of the material. In the latter method the total traction on the node is calculated by the sum of the traction from equation 4.1 and a viscous pressure term $t_v = c'(\alpha) \cdot v$, where c' is the damping coefficient (units $kg \cdot m^{-2} \cdot s^{-1}$) and v is the velocity of the relative velocity of the nodes.

$$c'(\alpha) = \begin{cases} 0 & \text{for } \alpha < -\alpha' \\ c'_0 \cdot (\alpha + \alpha') / (1-\eta) \cdot \alpha' & \text{for } -\alpha' \le \alpha < -\eta \cdot \alpha' \\ c'_0 & \text{for } \alpha \ge -\eta \cdot \alpha' \end{cases} \qquad \ldots (4.4)$$

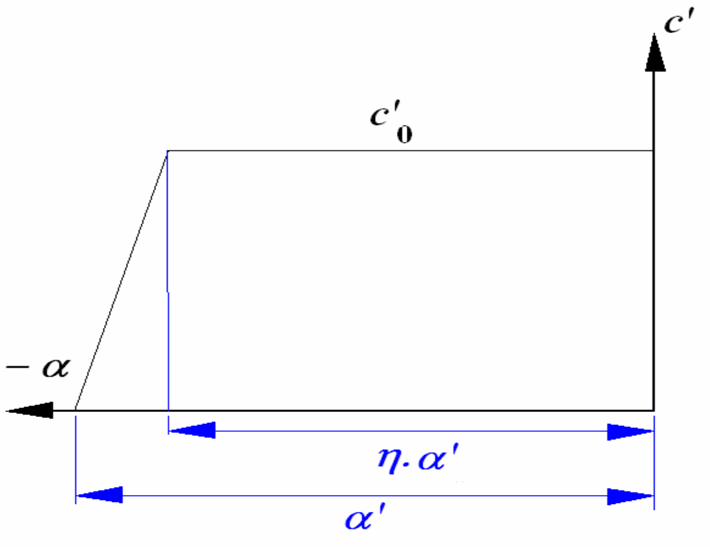

Fig 4.5: Viscous damping coefficient

The results show good agreement between the two different solver methods and serves to validate the subroutine developed. Any excess/incorrectly applied damping would have distorted the solutions – deviated from the results obtained in the Riks method (fig 4.6).

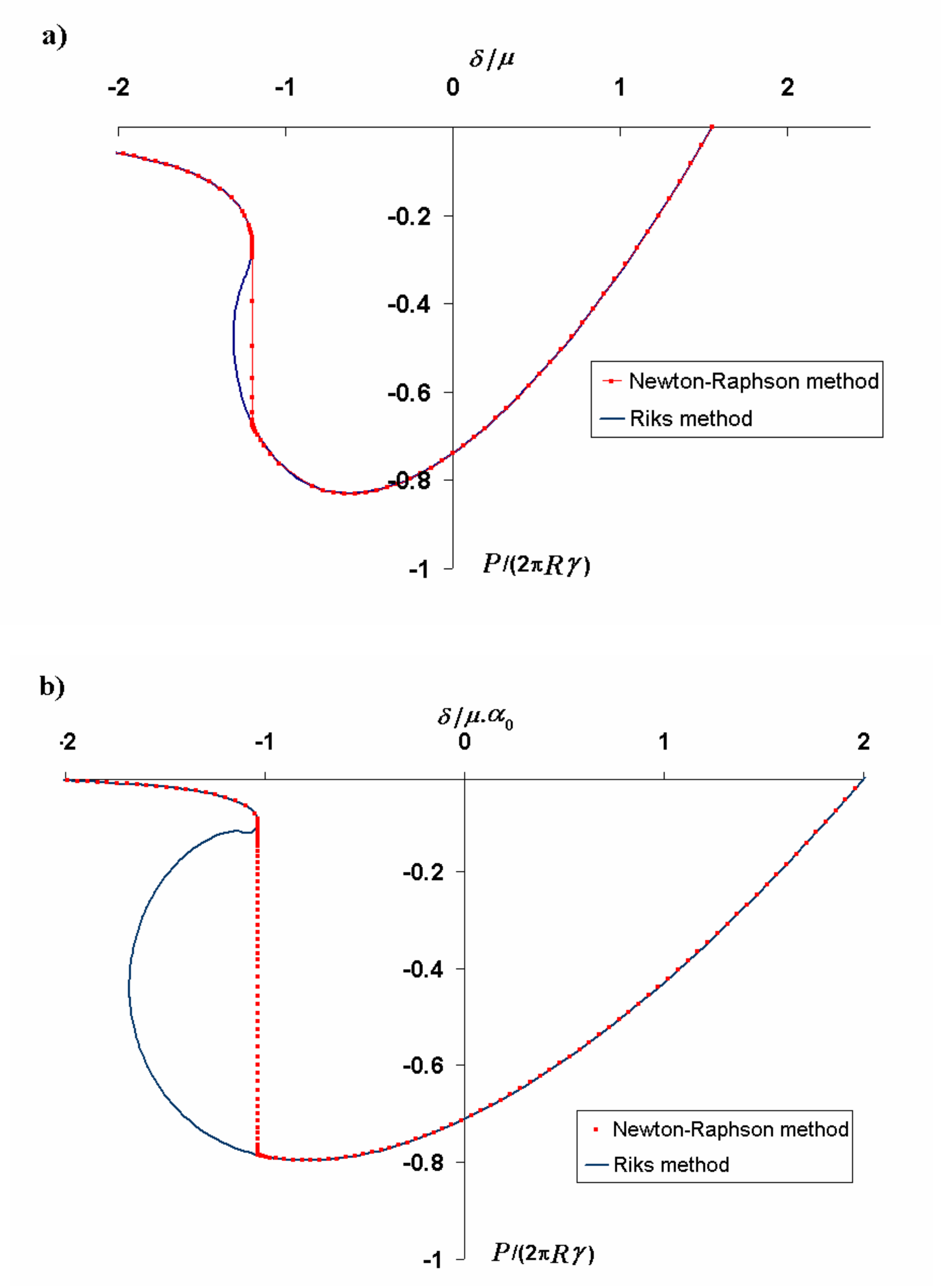

Fig 4.6: Load-depth curves[10] for a) $\mu = 0.75$ b) $\mu = 2.0$

---

[10] The contact law used here is LJP 10,4 (equation 4.10)

CHAPTER 5

A PHENOMENOLOGICAL MODEL FOR THE CARBON NANOTUBE TURF

The nanotube turf is a complex structure and an analysis of the mechanical behavior is complicated by the discrete nature of the turf. A rigorous analysis would involve each carbon nanotube to be modeled separately with appropriate contact laws. The sheer number of tubes and the complicated form of the contact law makes such an investigation daunting.

While a discrete analysis of the turf is desirable, deducing a simplified (continuum) model is more convenient and is based on certain experimental observations. Yurdumakan B. *et al* [26] reported that any pattern of a carbon nanotube turf grown on a silicon substrate could be peeled and transferred exactly to a blank polymer (PMMA) film. This property of the turf to retain its original structure when removed from the substrate implies the possibility of treating the turf as a material.

A proper continuum model of the nanotube turf should account for the non-linear elastic response and the time dependent relaxation of the material. Additionally, the analysis should also include a contact law to model the strong adhesion in the turf.

5.1 Phenomenological constitutive law

As seen earlier from the continuous-stiffness indentation experiments (fig 2.4), the turf exhibits a high, initial tangent modulus followed by an order of magnitude decay in its value with increasing deformation (strain). Based on these results, an idealized form of relation for the tangent modulus of the turf under uniaxial compression is devised.

$$E^t(\varepsilon) = d\sigma/d\varepsilon = E^0 \cdot e^{-\varepsilon/\varepsilon_0} + E^\infty \cdot (1 - e^{-\varepsilon/\varepsilon_0}) \qquad \ldots (5.1)$$

where E^t, is the tangent modulus, E^0 is the initial tangent modulus, E^∞ is the tangent modulus at large strains, ε is the nominal strain and ε_0 is the representative strain. The resulting uniaxial stress-strain curve computed from the above relation is shown in fig 5.1. The representative strain (ε_0) can be thought of as the parameter that controls the transition from E^0 to E^∞ .

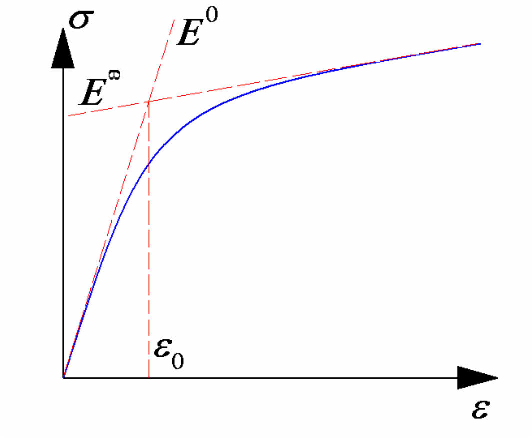

Fig 5.1: Uniaxial nominal stress-strain curve under compression

While the idealized relation for the tangent modulus in equation 5.1 closely resembles the experimental data, an appropriate non-linear elastic material with behavior similar to that in fig 5.1. is required for finite element analysis. An attractive form of hyper-elastic material for the current problem is a type of Green elastic material which is assumed to have a strain-energy potential (*U*) expressed in a polynomial form of the principal stretches with suitable powers. Such non-integer powers of stretches posses significant advantages and are often used to fit data from standard experiments (uniaxial, biaxial, volumetric tests) as well as to solve numerical problems (Storakers [22], Ogden [19]). Based on the assumed existence of the strain-energy function, the stresses are then given by

$$\sigma_i = dU/d\varepsilon_i \qquad \ldots (5.2)$$

where i = 1 to 6, σ_i and ε_i are conjugate, not necessarily tensorial, stress and deformation measures. A form of the energy potential frequently used to model highly compressible materials is given by (due to R. Hill [9])

$$U = \sum_{i=1}^{N} \frac{2\mu_i}{\phi_i^2}\left[\lambda_1^{\phi_i} + \lambda_2^{\phi_i} + \lambda_3^{\phi_i} - 3 + \frac{1}{\varphi_i}\left((J)^{\phi_i \varphi_i} - 1\right)\right] \qquad \ldots (5.3)$$

For the above form of energy function, the nominal stresses, conjugate to the principal stretches can be expressed as

$$\sigma_j = \frac{1}{\lambda_j}\sum_{i=1}^{N} \frac{2\mu_i}{\phi_i}\left(\lambda_j^{\phi_i} - J^{\phi_i \varphi_i}\right) \qquad \ldots (5.4)$$

where j = 1 to 3, and no summation over j is implied. There is assumed to exist, a ground-state (zero-stress state) with an initial shear and bulk modulus

$$\mu_0 = \sum_{i=1}^{N} \mu_i \quad ; \quad \kappa_0 = \sum_{i=1}^{N} 2\mu_i \left(\varphi_i + \frac{1}{3}\right) \qquad \ldots (5.5)$$

Here ϕ_i and μ_i are material parameters and $J = \lambda_1 \cdot \lambda_2 \cdot \lambda_3$, is the Jacobian of the deformation gradient tensor. The parameter ϕ_i determines the degree of compressibility of the material and is related to the Poisson's ratio by

$$v_i = \sum_{i=1}^{N} \frac{\varphi_i}{1 + 2\varphi_i} \qquad \ldots (5.6)$$

The summation for all the above expressions extends up to N terms and its value usually depends on the complexity of the experimental data used to fit the above relations. Most often one would require just one or two terms in the series to obtain a good quality fit.

For the carbon nanotube turf, due to the limited availability of data from experiments (only continuous-stiffness indentation tests), the following simplifications are made

i) The material is assumed to be isotropic (strain energy function is symmetric in its arguments i.e. $U(\lambda_1,\lambda_2,\lambda_3) = U(\lambda_2,\lambda_3,\lambda_1) = U(\lambda_3,\lambda_1,\lambda_2)$) although the actual material is orthotropic with five elastic constants. The isotropic assumption permits the use of the previously defined hyper-elastic material for analysis.

ii) As the turf is expected to be highly compressible, the Poisson's ratio is taken as zero but, in reality, the value is expected to be slightly higher.

Based on the above assumptions, the relation for the nominal stresses for the turf reduces to

$$\sigma_j = \frac{1}{\lambda_j}\sum_{i=1}^{N}\frac{2\mu_i}{\phi_i}\left(\lambda_j^{\phi_i} - 1\right) \qquad \ldots (5.7)$$

The values of ϕ_i and μ_i depend on the tangent modulii and representative strain chosen for the turf. While the turf has an initial tangent modulus ranging from 800 MPa to 300 MPa, the ratio, E^0 / E^∞ is almost constant for all cases (≈10). The exact values of all the above elastic constants will depend on the structural parameters of the turf (length of tubes, contacting segments; curvatures; modulus of the tubes etc). For the finite element analysis of the nanoindentation experiments, the following elastic properties were taken.

Initial tangent modulus, E^0 : 700 MPa

Tangent modulus at large strains, E^∞ : 70 MPa

Representative strains, ε_0 : 0.05, 0.075, 0.1, 0.15

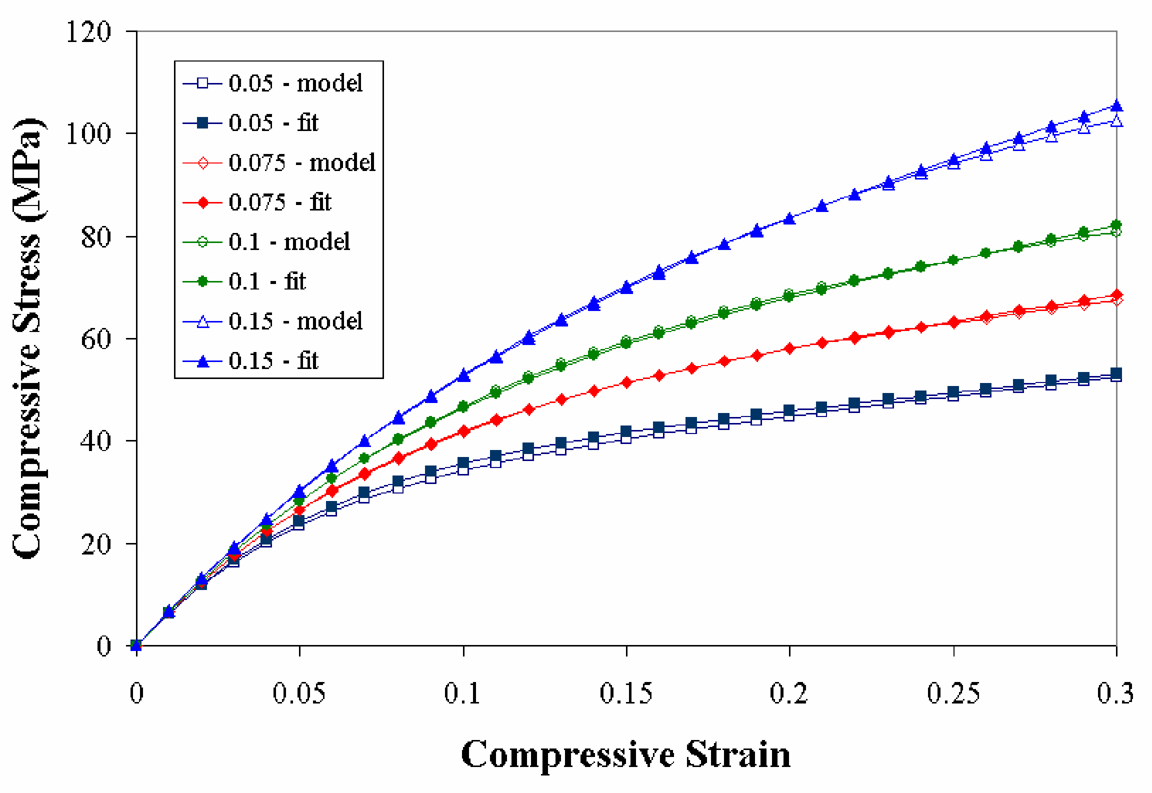

Fig 5.2: Uniaxial stress-strain curves under compression. The curves are computed for different values of representative strain (ε_0) using the equation 5.1 (shown as model – idealized experimental curve). A hyper-elastic material fit for the above is done using equation 5.7.

ε_0	μ (MPa)	ϕ	φ
0.05	350.0	18.8	0.
0.075	350.0	14.5	0.
0.1	350.0	12.0	0.
0.15	350.0	9.1	0.

Table 5.1: Elastic constants used to fit the (idealized) experimental data with the hyper-elastic model ($N = 1$).

As seen in the fig 5.2, the uniaxial stress-strain curves for the turf from the experiments and the corresponding hyper-elastic material for different ε_0 are in good agreement within the expected range of strains.

Another feature to be included in the material is the time dependent relaxation seen during the experiments (fig 2.2). This time dependence is due to the thermally activated sliding of contacts between the adjacent tubes. While the actual form of this dependence requires a more complicated analysis, a very simple relation is used here to model the relaxation. Here the instantaneous shear and bulk modulus are assumed to have identical relaxation coefficients and take the form

$$\mu(t) = \mu_0\left(1-\bar{\mu}\left(1-e^{-t/\tau}\right)\right) \qquad \dots (5.8)$$

where $\mu(t)$ is the instantaneous shear modulus, μ_0 is the initial shear modulus, τ is the characteristic relaxation time, $\bar{\mu} = (\mu_0 - \mu_\infty)/\mu_0$ and μ_∞ is the relaxed shear modulus.

5.2 Phenomenological contact law

As seen earlier in fig 2.2 and the previous chapter, the strong adhesion between the turf and the Berkovich tip must be taken into account for interpreting the data from the standard indentation test experiments. While the adhesion law for linear-elastic solids (fig 3.4) was modeled based on the idealized Lennard-Jones potential, the contact law for the turf is complicated by the thermal vibrations. The nanotube turf has free standing tubes at the surface of the turf. These tubes being slender (length>>diameter) and compliant, tend to vibrate about their mean position due to the thermal vibrations of the carbon atoms.

For determining the magnitude of vibration at the tip, each tube is assumed to be a homogeneous hollow cylinder of length l, inner and outer radii r_i and r_o respectively. Further the tube is assumed to be firmly fixed at one end (displacement and slopes are zero). While the nanotube can vibrate both in longitudinal and transverse directions, only the displacement in transverse direction is significant and hence only it is considered. The droop due to gravity being small is also neglected. With the above considerations, the root mean square of the nanotube tip displacement can then be shown as [24]

$$u \approx \left(0.4243 \frac{l^3 kT}{Y\left(r_o{}^4 - r_i{}^4\right)} \right)^{1/2} \qquad \ldots (5.9)$$

where k is the Boltzmann's constant, Y is the elastic modulus of a single nanotube. Using the following values l = 7 μm, T = 300 K, Y = 0.4 TPa, r_o = 20 nm, r_i = 17.3 nm, the displacement at the end of the tube is determined ($u \approx 5$ nm). A specific form of Lennard

Jones potential commonly used to model the interaction between carbon atoms (due to Zhao and Spain [27]) is given by

$$t(\alpha) = \left(\frac{36.5}{6}\right)\left(\left(\frac{\alpha_0}{\alpha}\right)^{10} - \left(\frac{\alpha_0}{\alpha}\right)^{4}\right) \qquad \dots (5.10)$$

where the traction ***t*** is in GPa and the value for the inter-atomic equilibrium distance α_0 is 0.34 nm. In the current analysis the indenter is a diamond tip and hence the interaction between the indenter and turf is modeled based on the above law. The contact law ignores the presence of any impurities/foreign particles like catalyst, etc. As the above interaction law does not account for thermal vibrations of the atoms, it is modified to account for the nanotube end displacement. The total surface energy is kept the same (area under the curve) while the curve is translated so that the intercept from the zero curvature (α_{int}) on the x-axis is shifted by a value equal to u (fig 5.3).

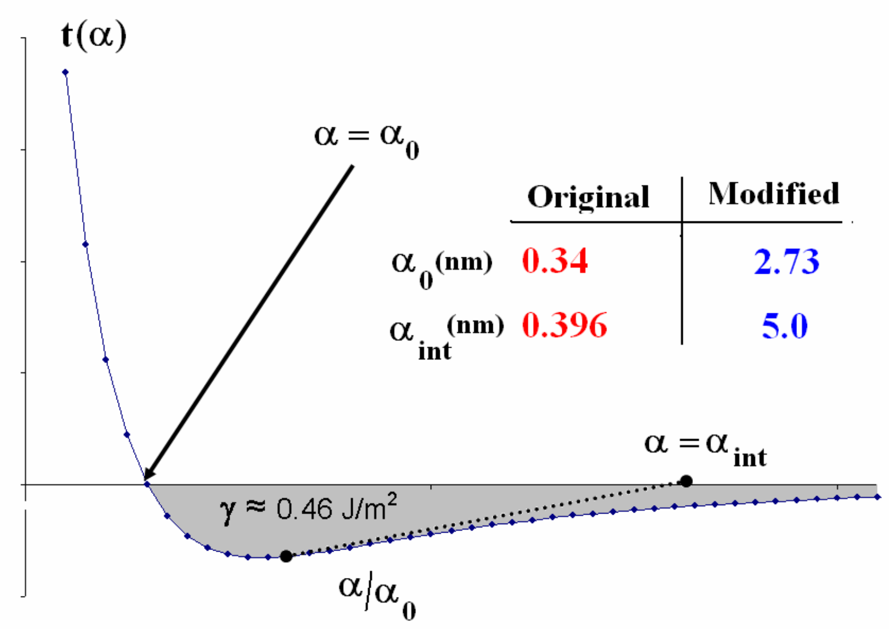

Fig 5.3: Original interaction law (from equation 4.10), modified law

CHAPTER 6

DISCUSSION ON THE RESULTS

The results from the finite element analysis are broadly divided into two sections. First the results from the adhesion in linear elastic spheres are discussed followed by the results from the simulation of the indentation experiments on the turf.

6.1 Adhesion in linear elastic spheres

It is interesting to look back at the equation 3.4 from the JKR theory. The contact radius a can be expressed as a function of the indenter load P or the indenter displacement δ. The former case refers to a load controlled experiment and the latter a displacement controlled experiment. In an ideal controlled load experiment, the spring stiffness K is assumed to be zero while in an ideal controlled displacement experiment, K is infinite. In reality, the stiffness of the spring is finite so the slope of the load-displacement curve during the jump is equal to the stiffness of the spring ($K = \Delta P / \Delta \delta$). Also evident from the figure 6.1, is that the adhesion process is a non-conservative i.e. an additional amount work needs to be expended so as to cause complete separation of the surfaces during the retraction process. During the jump (vertical line), energy is dissipated (lost) in an elastic wave motion in the solids [12].

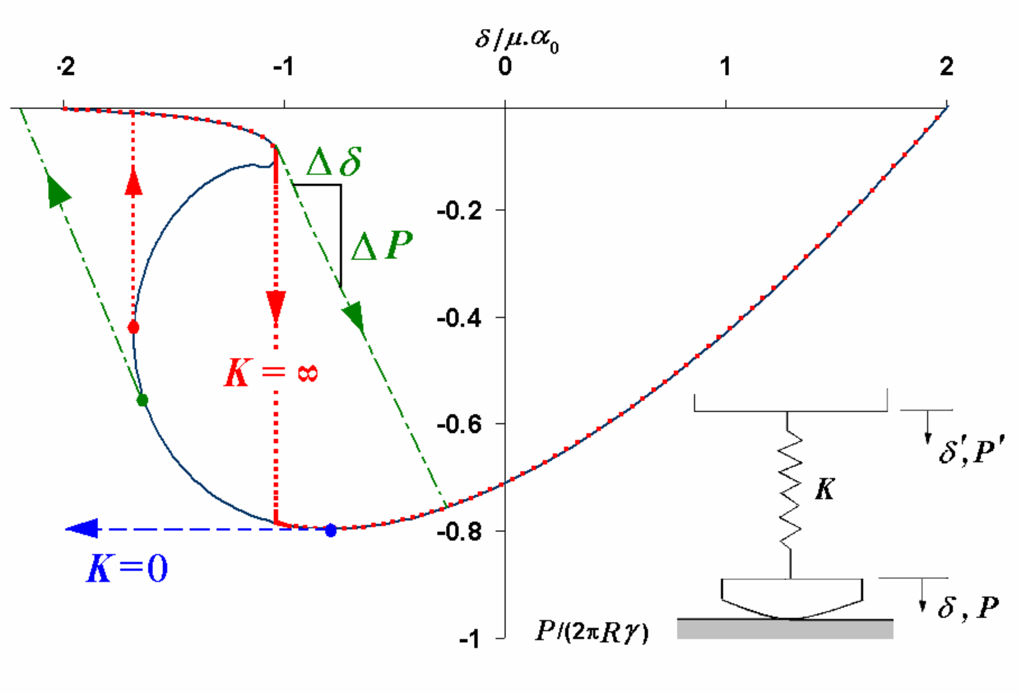

Fig 6.1: Load-displacement curve for different spring stiffness (*K*), *μ*=2.0. (inset) Typical indentation mechanism (primed variables are controlled parameters).

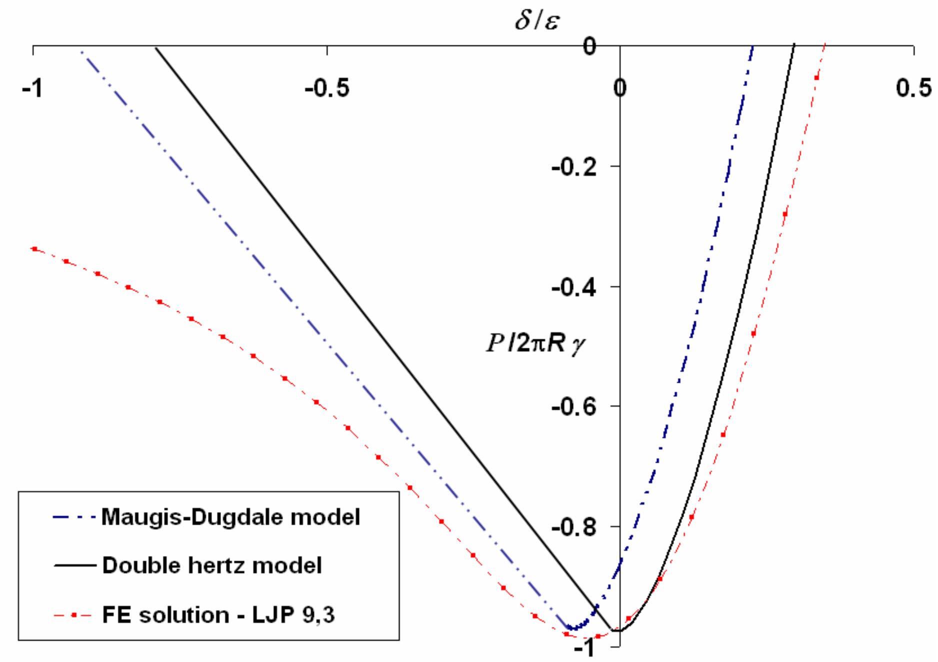

Fig 6.2: Load-depth curves for μ =0.1 Note: While the pull-off load values are almost identical, the load-approach curves vary due to different interaction laws used.

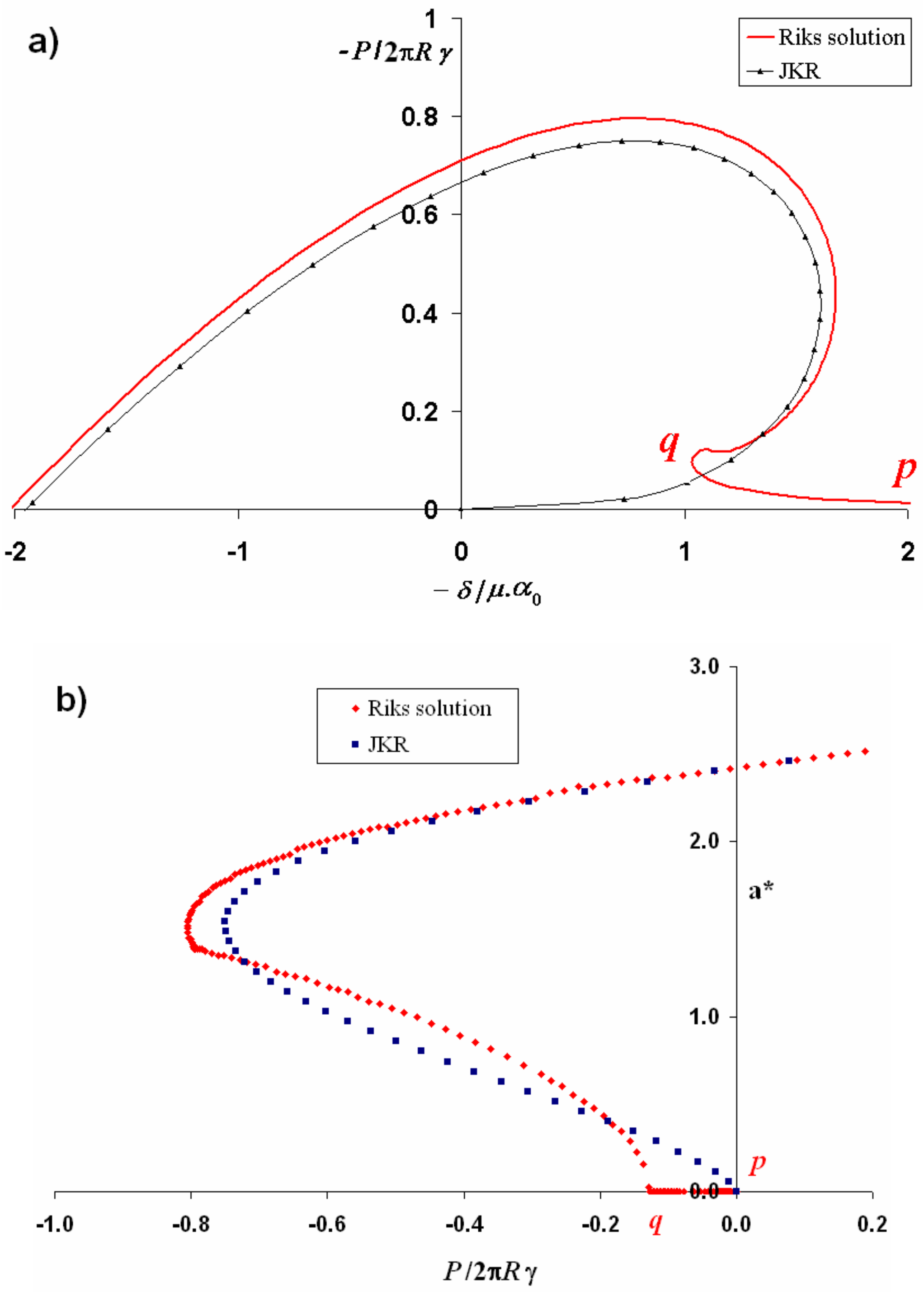

Fig 6.3: Comparison of the solution from Riks method with the JKR solution ($\mu = 2$)

a) Load-depth curves b) Load-contact area curves – the contact area a is normalized with the typical contact area at zero load a', $a^* = a/a'$ where $a' \propto \left(R^2\gamma/E^*\right)^{1/3}$

Interestingly when the load-depth curves are compared with the JKR theory (fig 6.3a), initially it looks like there is no similarity between the numerical results and the JKR theory (segment *p*-*q*). The reason is that the JKR theory is a surface analysis approach and it assumes that there is always a contact between the two surfaces. On the other hand, the finite element analysis shows that initially during the segment *p*-*q*, there is no contact between the two surfaces and once the point *q* is reached, contact is established (fig 6.3b). At that point, the load-displacement curve sweeps back to form an envelope around the JKR curve and hence we see the 'inverted S-shaped' curve. Current theories [6, 7 and 13] predict that as the value of μ increases, the load-depth curves start approaching the JKR curve as if it were a limit. While the goal was to capture such a trend using finite element analysis, the results were very surprising (fig 6.4)

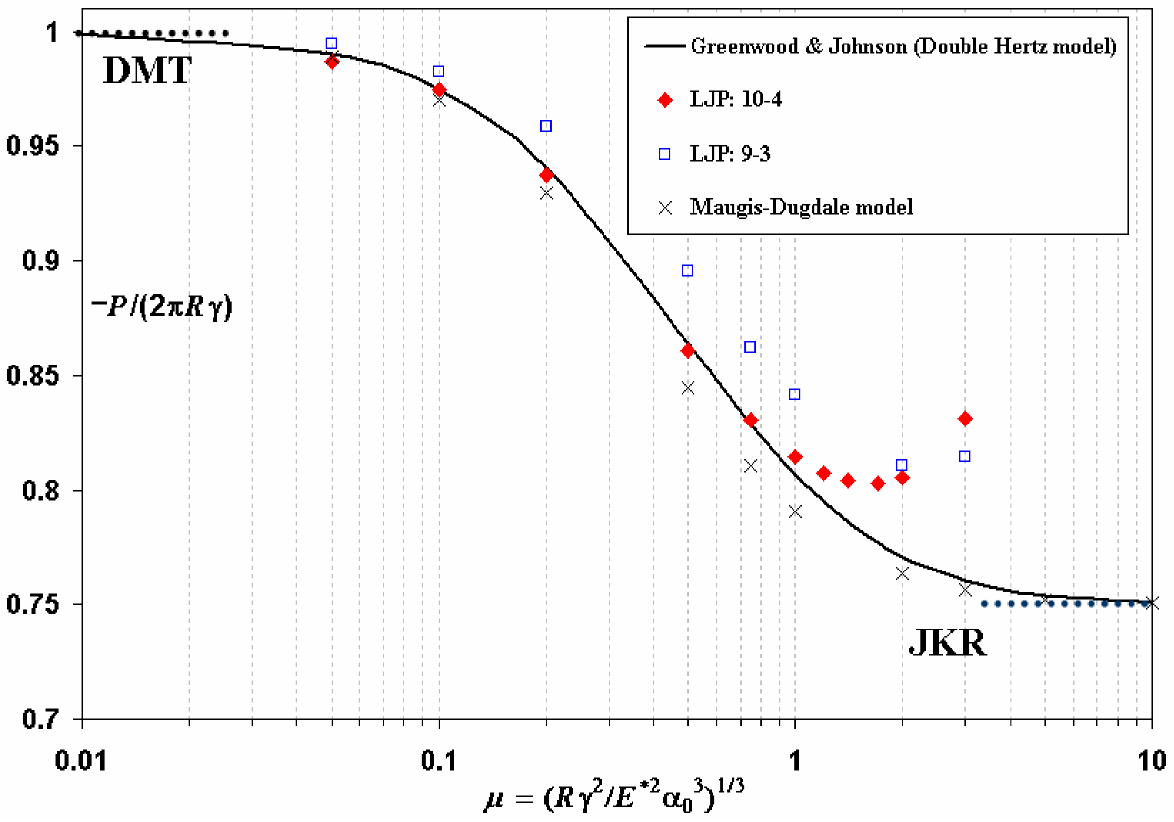

Fig 6.4: Pull-off load values for different μ.

When the pull-off load values from the finite element results using two forms of contact law: LJP 10,4 and LJP 9,3 were compared with the existing theories, it was found that they do not approach the JKR limit. Rather they showed an increasing trend from ($\mu > 2$). This feature was surprising for, at least till now, it was thought that the mechanism of adhesion in linear elastic solids was well understood. While the results from the finite element analysis were initially looked at with skepticism, it was later realized that there could be a feature that was probably not taken into account in the existing theories. All the work till now assumes that the displacement gradients are small (small strains and small rotations). This assumption allows the use of the principle of superposition to determine the stresses in the contacting bodies – eg. Maugis-Dugdale model and the Double-Hertz model.

In reality, as the value of μ increases (or as the material becomes softer[11]), the strains are still small, but the rotations are large[12]. The maximum slope of the deformed profile increases exponentially and thus the contact becomes more of a blunt crack tip. Although the existing theories predict the same trend, the deformed profile outside the contact radius is incorrectly determined. This leads to the incorrect determination of the tractions outside the contact area and hence the load on the spheres. The finite rotations void the use of the principle of superposition to determine the solutions. Instead, one must rely on a numerical technique to solve for the stresses in the adhering materials. While Greenwood [6], Attard and Parker [2] used a numerical technique to solve for the

---

[11] The increase in the value of the Tabor's parameter μ can be thought of as increasing the compliance ($1/E^*$) of the material by keeping the other parameters (R, $\gamma_{,\square 0}$) constant

[12] A familiar problem of this type is the end loading of a slender cantilever beam. The strains are small but rotations are large.

stresses, they did so by using elliptic integrals, implying the use of the small deformation gradient assumption.

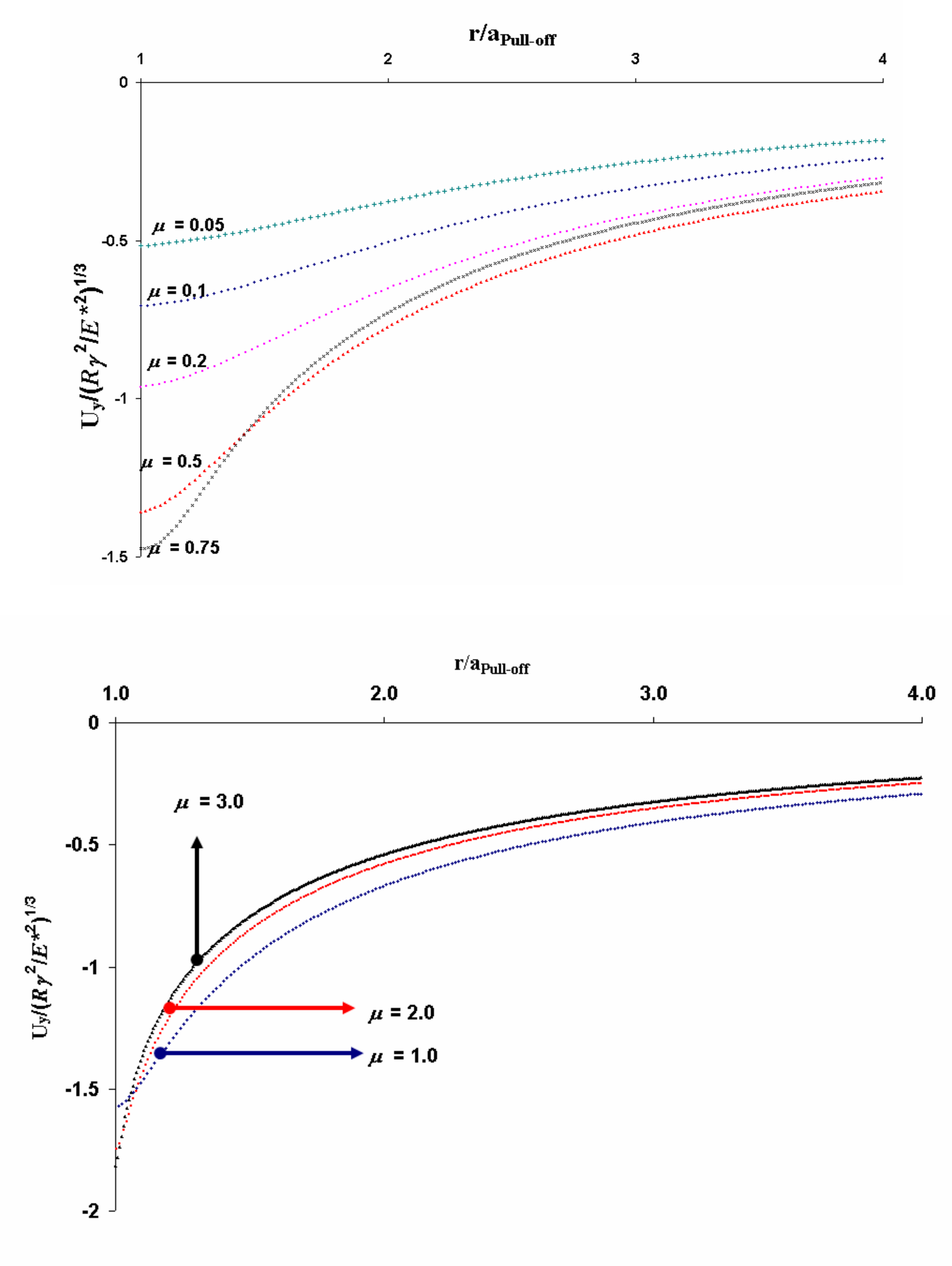

Fig 6.5: Deformed profile outside the contact radius at the pull-off load

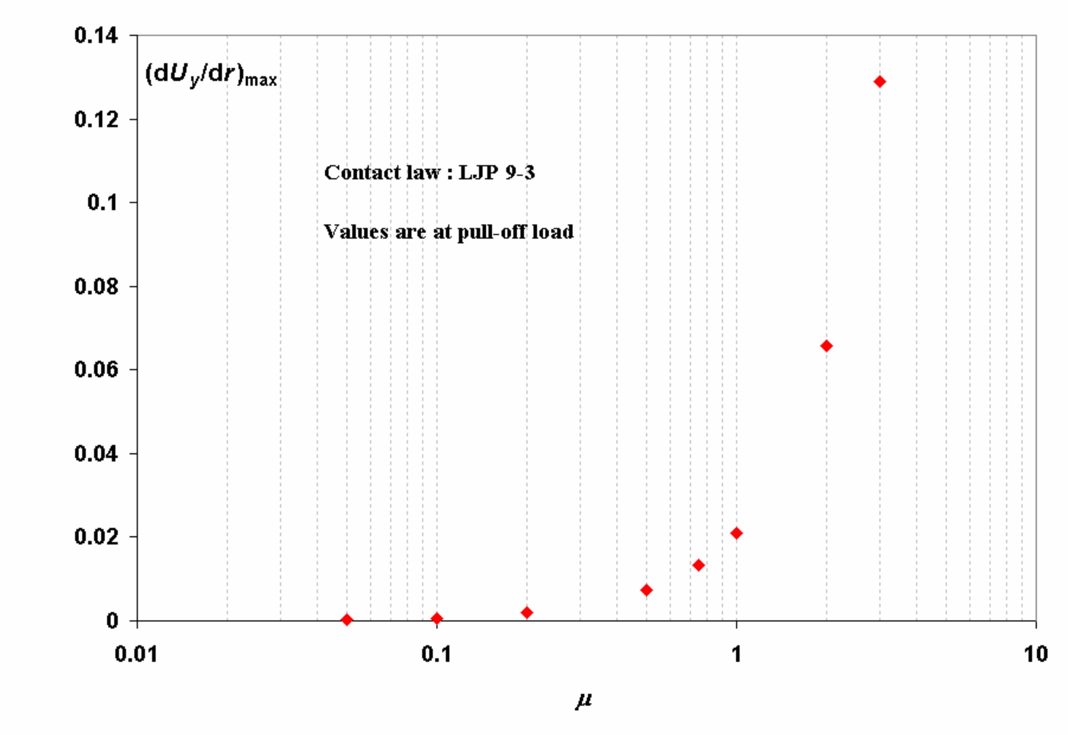

Fig 6.6: Maximum slope of the deformed profile outside the contact radius

6.2 Simulation of the indentation experiments on the carbon nanotube turf

Here the turf is modeled as a continuum and is discretised using 3-noded axis-symmetric triangular elements (28,397 elements). The mesh is biased, with a very fine mesh close to the contact area while elements at a distance from the contact are much larger. The total width of the turf is more than ten times the contact radius. The material properties (fig 5.2) are defined using the *HYPERFOAM option, while the contact law (fig 5.3) is specified using the user subroutine UINTER [1]. The analysis was performed for different values of representation strain (ε_0) and different relaxation ratios $(\bar{\mu})$. The indentation mechanism modeled is similar to that in fig 6.1 (K = 1 μN/nm).

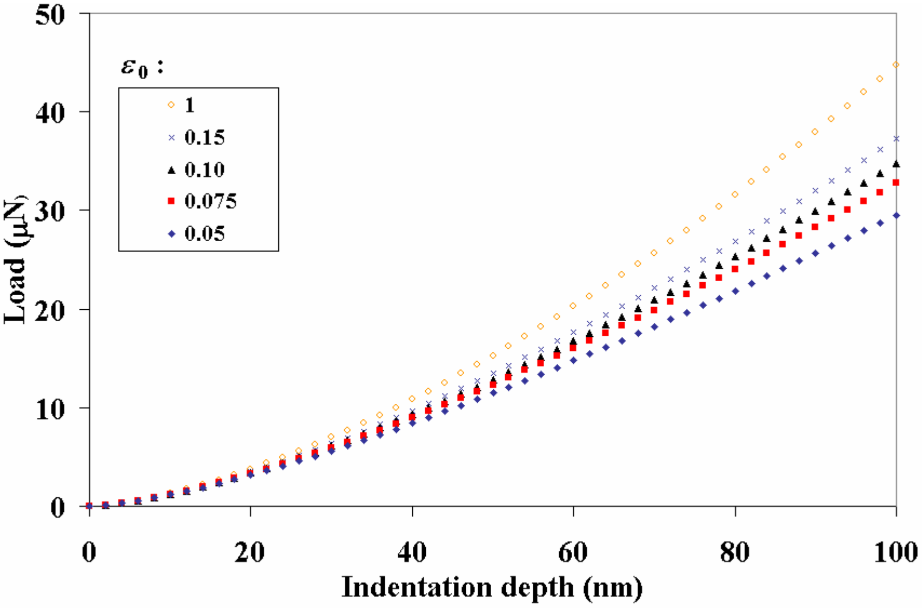

Fig 6.7: Load-depth curves for the turf with no relaxation and adhesion. The curve, $\varepsilon_0 = 1$ refers to a linear-elastic material

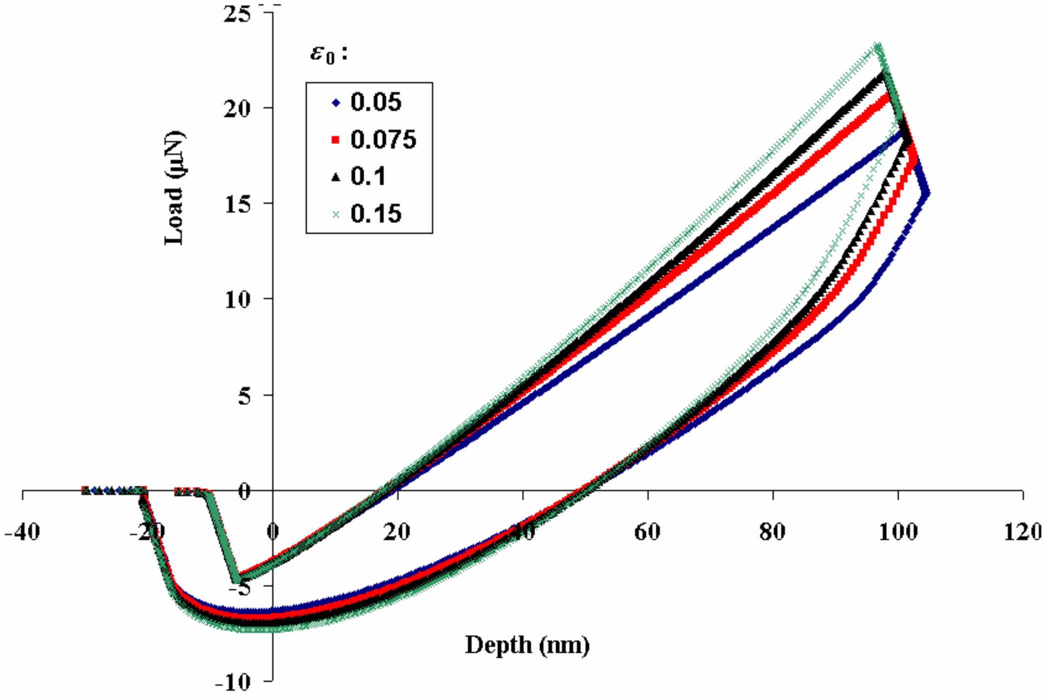

Fig 6.8: Displacement controlled analysis with a loading/unloading rate of 10nm/sec, Load-depth curves. Relaxation and adhesion are modeled. $\bar{\mu} = 0.4$, $\tau = 3$ seconds

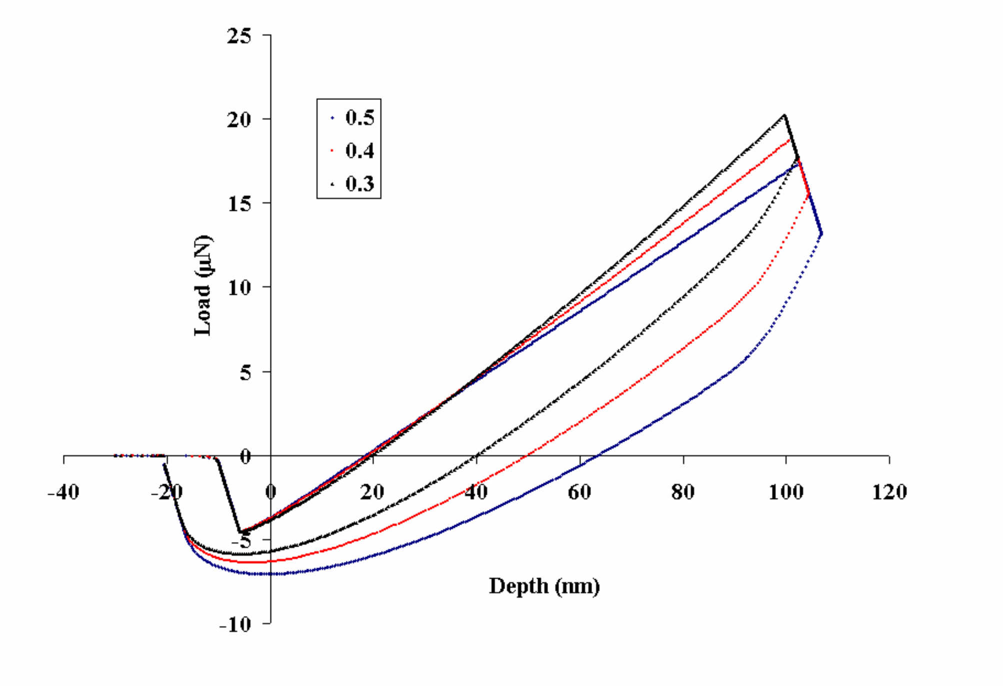

Fig 6.9: Displacement control analysis: Load-depth curves for ε_0=0.05, different $\bar{\mu}$, τ= 3 seconds

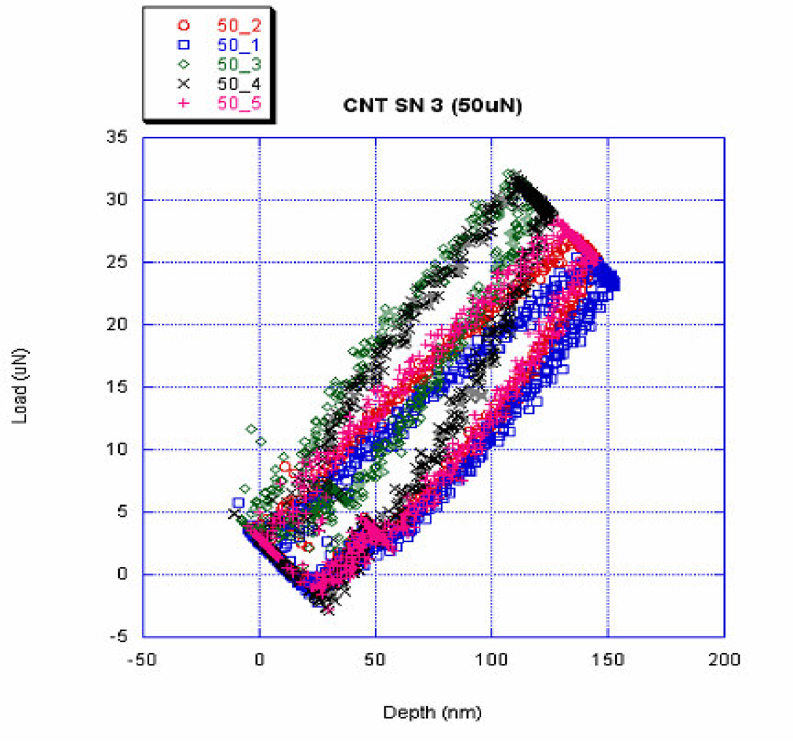

Fig 6.10: Experimental results at different points on the turf

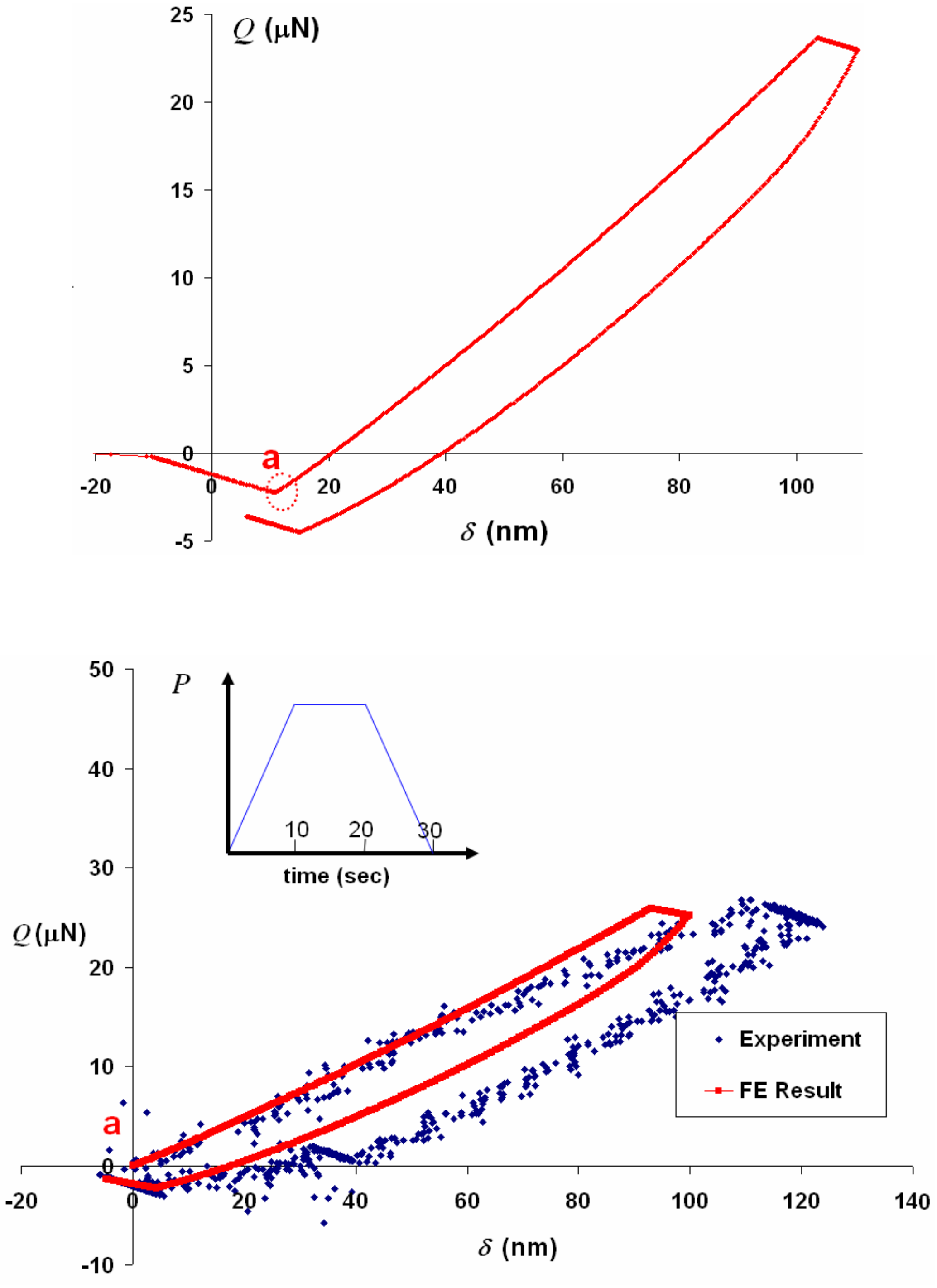

Fig 6.11: Load control analysis on the turf. The FE result (top) is edited so that the point ‘a’ is made to coincide with the zero load, zero displacement point. The loading mechanism is similar to that in fig 2.1a with (k_1 =210 mN/nm, k_2 = 100 nN/nm). ε_0=0.05, $\bar{\mu}$ =0.4, τ = 3s

While the control displacement analysis demonstrates the jump-to-contact and pull-off behavior of the turf, an additional run was done to mimic the actual loading on the turf – control load analysis (fig 6.11). The results from the finite element analysis were able to predict a *roughly* linear load-depth relation during the loading cycle. Also, the pull-off loads during the retraction of the spherical indenter from the turf closely matched the experiments. An important feature is that the experimental data starts with a positive indenter load. This is due to the experimental difficulty in locating the top surface of the turf – hence the tensile load on the indenter during the loading phase is not seen. It is crucial to highlight the limitations of the current continuum model.

1. The material is assumed to be isotropic, while the actual turf is orthotropic. Determining the material constants for the turf is difficult due to the limited types of experiments that can be done on the turf. An indirect way to determine the material properties is to develop a complicated micro-mechanical model of the turf, where each carbon nanotube is modeled as a spatial elastica with appropriate laws for contact between adjacent tubes. A relation to link the parameters from the micro-mechanical model with the continuum model also needs to be developed.

2. The Poisson's ratio of the material is taken as zero. The actual value could be higher as evident from fig 2.4. The experiments conducted at different locations on the turf show varying tangent modulus curves. The lower tangent modulus curves are expected for tests done near the edge of the turf.

3. A realistic contact law between the turf and the indenter tip must also include time dependence – creep in the contact radius under constant load/depth. The mechanism of creep is thought to be due to the sliding of contacts between the contacting tubes. As modeling of this behavior in the contact law is rather tedious, the time dependent behavior is modeled solely as the material property of the turf.

4. The contact law for the turf developed assumes that the turf has a flat surface. The actual turf has a very rough surface as seen from the results form the AFM experiment (fig 6.12). The surface is jagged, with the vertical distance between the trough and the peak about 1 μm. This makes it extremely difficult to define a surface for the actual turf and the rough nature increases the range of the adhesive forces. Yurdumakan *et al* [26] reported that inverting the turf produces a smooth surface and the range of adhesive forces actually drops significantly when compared with the initial rough surface (tens of nanometers compared to the 1 μm range seen here.

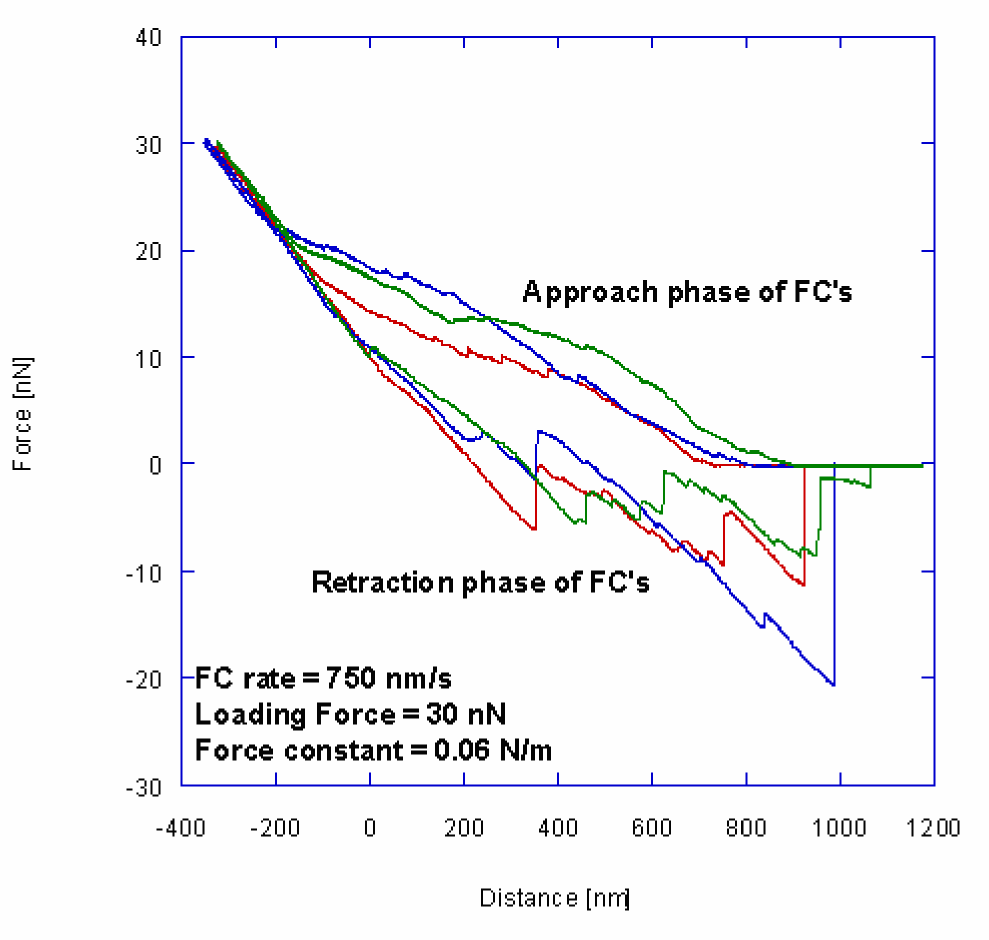

Fig 6.12: Typical force curve for a long thin AFM cantilever (**courtesy:** Koneswaran Sinnathamby, Haijun Ma and Christopher M. Yip of the University of Toronto)

CHAPTER 7

CONCLUSIONS

The mechanical behavior of the turf is characterized by

i) Nonlinear elasticity with a sharp decrease in the tangent modulus with strain

ii) Small viscoelastic relaxation

The physical mechanism responsible for the time dependent relaxation of the turf is the thermally activated sliding of contacts between the adjacent nanotubes. The sharp drop in the tangent modulus of the turf is the consequence of the built-in bending strain energy of the turf. The total initial energy of the turf is minimized by a particular combination of the bending strain energy and contact energy. While the turf will have multiple energy minima with broad convex regions, absolute energy minima is expected when all the nanotubes collapse laterally and are in contact along the entire length.

The phenomenological model for the carbon nanotube turf is developed assuming isotropy and a Poisson's ratio of zero (reflecting the high compressibility of the turf). The strong van der Waals forces between the indenter and the turf are modeled by modifying the Lennard Jones type interaction law to account for the thermal vibrations at the tip of the nanotube. Owing to the thermal vibrations, the adhesive forces between the turf and the indenter are expected to have a longer range than the atomic forces. The time dependent relaxation for the material is modeled similar to that of a linear viscoelastic solid and assuming the instantaneous bulk and shear modulus have the same relaxation coefficient. The finite element results of the spherical indentation on the carbon nanotube turf displayed the various features seen during the experiments (linear load-depth response, time dependent relaxation and pull-off load characteristics). The determination of the orthotropic material properties of the turf still remains an open issue and may be possible by a more rigorous ‘discrete’ analysis of the structure.

The strong adhesion seen during the standard indentation experiments warranted a study on the existing theories of adhesion. To benchmark the developed contact algorithm in the finite element model, runs were done to compare the results with existing theories of adhesion. While the existing models predict the pull-off load values approach the JKR value as a limit with increasing μ, the finite element model developed predicted an increasing trend of the normalized pull-off load from $\mu \approx 2$. This discrepancy between the two results is due to the neglecting of finite deformation in the elastic half-space by the existing models.

REFERENCES

1) ABAQUS manuals 6.5, 2005. ABAQUS Inc., Pawtucket, RI.

2) Attard P., Parker J.L., Deformation and adhesion of elastic bodies in contact, *Phy. Rev. A,* **46**, No. 12, 7959-7971 (1992)

3) Bernholc J., Brenner D., Buongiorno Nardelli M., Meunier V., Roland C., Mechanical and electrical properties of nanotubes, *Annu. Rev. Mater. Res.*, **32**, 347-375 (2002)

4) Cao A., Dickrell P.L., Sawyer W.G., Ghasemi-Nejhad M.N., Ajayan P.M., Super-compressible foamlike carbon nanotube films, *Science*, **310**, 1307-1310 (2005)

5) Derjaguin B.V., Muller V.M., Toporov Yu. P., Effect of contact deformations on the adhesion of particles, *J. Coll. Interf. Sci.*, **53**, 314-326

6) Greenwood J.A., Adhesion of elastic spheres, *Proc. R. Soc. Lond. A.*, 453, 1277-1297 (1997)

7) Greenwood J.A., Johnson K.L., An alternative to the Maugis model of adhesion between elastic spheres, *J. Phys. D: Appl. Phys.*, **31**, 3279-3290 (1998)

8) Greenwood J.A., Johnson K.L., Oscillatory loading of a viscoelastic adhesive contact, *J. Coll. Int. Sci.*, **296**, 284-291 (2006)

9) Hill R., Aspects of Invariance in Solid Mechanics, *Adv. Appl. Mech.*, **18**, 1-75 (1978)

10) Johnson K.L., Kendall K., Roberts A.D., Surface energy and the contact of elastic solids, *Proc. R. Soc. Lond. A*, **324**, 301-313 (1971)

11) Johnson K.L, Contact Mechanics, *Cambridge University Press* (1985)

12) Johnson K.L., Greenwood J.A., An adhesion map for the contact of elastic spheres, *J. Coll. Int. Sci.*, **192**, 326-333 (1997)

13) Maugis D., Adhesion of spheres: The JKR-DMT transition using a Dugdale model, *J. Coll. Int. Sci.*, **150**, No. 1, 243-269 (1992)

14) McCarter C.M., Richards R.F., Mesarovic S., Richards C.D., Bahr D.F., McClain D., Jiao J., Mechanical compliance of photolithographically defined vertically aligned carbon nanotube turf, *J. Mater. Sci.* (In press)

15) Mesarovic S.Dj., Fleck N.A, Spherical indentation of elastic-plastic solids, *Proc. R. Soc. Lond. A.*, **455**, 2707-2728 (1999)

16) Mesarovic S.Dj., Johnson K.L., Adhesive contact of elastic-plastic spheres, *J. Mech. Phys. Solids,* **48**, 2009-2033 (2000)

17) Mesarovic S.Dj., McCarter C.M., Bahr D.F., Radhakrishnan H., Richards R.F., Richards C.D., McClain D., Jiao J., Mechanical behavior of a carbon nanotube turf, *To appear in Scripta Mat.* (2006)

18) Miyazaki Y., Analytical solution of spatial elastica and its application to kinking problem, *Int. J. Solids Structures*, **32**, No. 27, 3619-3636 (1997)

19) Ogden, R.W., Large deformation isotropic elasticity – on the correlation of theory and experiment for incompressible rubberlike solids, *Proc. R. Soc. Lond. A.*, **326**, 565-584 (1972)

20) Pantano A., Parks D.M., Boyce M.C., Mechanics of deformation of single- and multi-walled carbon nanotubes, *J. Mech. Phys. Solids*, **52**, 798-821 (2004)

21) Qi H.J., Teo K.B.K., Lau K.K.S., Boyce M.C., Milne W.I., Robertson J., Gleanson K.K., Determination of mechanical properties of carbon nanotubes and vertically aligned carbon nanotube forest during nanoindentation, *J. Mech. Phys. Solids*, **51**, 2213-2237 (2003)

22) Storakers B., On material representation and constitutive branching in finite compressible elasticity, *J. Mech. Phys. Solids*, **34**, 125-145 (1986)

23) Tabor D., Surface forces and surface interactions, *J. Coll. Int. Sci.*, **58**, No. 1, 2-13 (1977)

24) Treacy M.M.J., Ebbesen T.W., Gibson J.M., Exceptionally high Young's modulus observed for individual carbon nanotubes, *Nature*, **381**, 678-680 (1996)

25) Waters J.F., Riester L., Jouzi M., Guduru P.R., Xu J.M., Buckling instabilities in multiwalled carbon nanotubes under uniaxial compression, *Appl. Phys. Lett.*, **85**, No 10, 1787-1789 (2004)

26) Yurdumakan B., Raravikar N.R., Ajayan P.M., Dhinojwala A., *Chem. Comm.*, 3799-3801 (2005)

27) Zhao Y.X., Spain I.L, X-ray diffraction data for graphite to 20 GPa, *Phy. Rev. B.,* **40**, No. 2, 993-997 (1989)